Journal Pre-proof

Influence of Ho^{3+} and Yb^{3+} Concentration Distributions on Ce^{3+}-Fine-Tuned Upconversion Luminescence in Highly Doped Core–Multi-Shell Upconversion Nanoparticles

Ye Kuang, Junhao Xu, Guangli Shi, Tengbo Hu, Xian Wang, Bo Li, Yu Liang, Panpan Qin, Wen Zeng, Hao Wang, Longhai Shen, Yiwei Wang

PII: S0925-8388(25)03488-7

DOI: https://doi.org/10.1016/j.jallcom.2025.181927

Reference: JALCOM181927

To appear in: *Journal of Alloys and Compounds*

Received date: 27 February 2025
Revised date: 17 June 2025
Accepted date: 28 June 2025

Please cite this article as: Ye Kuang, Junhao Xu, Guangli Shi, Tengbo Hu, Xian Wang, Bo Li, Yu Liang, Panpan Qin, Wen Zeng, Hao Wang, Longhai Shen and Yiwei Wang, Influence of Ho^{3+} and Yb^{3+} Concentration Distributions on Ce^{3+}-Fine-Tuned Upconversion Luminescence in Highly Doped Core–Multi-Shell Upconversion Nanoparticles, *Journal of Alloys and Compounds,* (2025) doi:https://doi.org/10.1016/j.jallcom.2025.181927

Influence of Ho^{3+} and Yb^{3+} Concentration Distributions on Ce^{3+}-Fine-Tuned Upconversion Luminescence in Highly Doped Core–Multi-Shell Upconversion Nanoparticles

Ye Kuang,[a,⊥] Junhao Xu,[b,⊥] Guangli Shi,[c] Tengbo Hu,[b] Xian Wang,[a] Bo Li,[a] Yu Liang,[a] Panpan Qin,[a] Wen Zeng,[a] Hao Wang,[a] Longhai Shen[b,*], and Yiwei Wang[d,e,*]

[a] College of Materials Science and Engineering, Shenyang Ligong University, Shenyang 110159, P. R. China
[b] College of Science, Shenyang Ligong University, Shenyang 110159, P. R. China
[c] Zolix Instruments Co., Ltd, Beijing 101102, P. R. China
[d] Department of Molecular Morphology Laboratory, Shenyang Medical College, Shenyang, 110034, P. R. China
[e] Liaoning Province Key Laboratory for Phenomics of Human Ethnic Specificity and Critical Illness, Shenyang, 110034, P. R. China
[*] Corresponding author
Corresponding author email addresses: shenlonghai@sylu.edu.cn, wangyiwei@symc.edu.cn
[⊥] Ye Kuang and Junhao Xu contributed equally

Abstract

Although widely used for Ho-based upconversion luminescence (UCL) fine-tuning of upconversion nanoparticles (UCNPs), Ce^{3+} doping has lacked comprehensive investigation in core–multi-shell and highly doped structures. Herein, a series of highly doped core–multi-shell UCNPs with Ce^{3+} doping were synthesised via oleate-based methods. The structures and morphologies were characterised by X-ray diffraction (XRD), transmission emission microscopy (TEM) and elemental mapping, while UCL properties were assessed using emission spectra, decay curves and pump power measurements. The distributions of Ho^{3+} and Yb^{3+} concentrations were systematically varied to explore, for the first time, their distinct effects on Ce^{3+}-mediated UCL fine-tuning. These effects arose from different energy mechanisms and varied with the number of shell layers. A deficiency in phonon energy was found to reduce the efficiency of both Yb^{3+}–Ho^{3+} energy transfer and Ho^{3+}–Ce^{3+} cross-relaxation while also exacerbating surface energy quenching. Beyond mitigating the phonon energy shortage and providing greater shielding for surrounding Ho^{3+} ions, a low Ho^{3+} concentration in the core and a high concentration in the first shell (S_1) were found to reduce the overall distance between Yb^{3+} and activated Ho^{3+} ions, enhancing energy transfer but increasing surface quenching. A high Yb^{3+} concentration in the second shell (S_2) and a low concentration in the third shell helped to promote inward sensitising energy transfer and suppress surface quenching, though this configuration partially intensified the phonon energy shortage. UCNPs with the composition $NaHoF_4$:10%Ce^{3+},40%Gd^{3+}@$NaHoF_4$:10%Ce^{3+}@$NaGdF_4$:10%Ce^{3+},60%Yb^{3+}@$NaGdF_4$:20%Yb^{3+} demonstrated optimal performance, exhibiting a red UCL decay time of 164.97 μs, a green-to-red intensity ratio of 0.43 and a quantum yield of 1.23%. Both metrics declined when Ce^{3+} dopants were confined only to S_2. Multi-layer Ce^{3+} doping outperformed configurations with doping limited to

the core or S_1. Moreover, the emission colour of Ce^{3+}-doped UCNPs remained tunable with variations in pump power. These findings provided valuable theoretical guidance for the design of Ce^{3+}-doped and highly doped UCNPs and enhanced the multifunction potential of $NaHoF_4$-based materials.

Keywords: $NaHoF_4$, upconversion nanoparticles, Ce^{3+}, concentration, highly doped, core–multi-shell, luminescence finetuning

Introduction

Rare-earth (RE) ions possess rich ladder-like energy levels that enable emissions across the ultraviolet, visible and near-infrared spectral regions. In upconversion luminescence (UCL) processes under 980-nm excitation, the $^2F_{5/2}$ state of Yb^{3+} ions aligns well with those of commonly used luminescent centres (Ho^{3+}, Er^{3+} and Tm^{3+}), facilitating efficient energy transfer (ET).[1-3] RE-doped upconversion nanoparticles (UCNPs) are an emerging class of optical nanomaterials exhibiting anti-Stokes emission and hold promise for a wide array of applications, including super-resolution nanoscopy,[4, 5] solar energy conversion,[6, 7] optical anti-counterfeiting,[8-10] deep-tissue imaging[11-13] and nanoscale temperature sensing.[14-16] Thanks to their low toxicity, superior photostability, sharp emission bands (<10 nm), long luminescent lifetimes (μs–ms) and large Stokes shift, UCNPs are considered more desirable than organic fluorescent dyes and quantum dots.[17-21]

However, the high surface-to-volume ratio inherent to nanoscale materials leads to significant surface energy quenching, substantially reducing UCL intensity and quantum yield compared to bulk materials.[22, 23] For instance, UCNPs with an average size of 8–10 nm exhibit quantum yields as low as 0.005%, larger particles (≥10 nm) and bulk crystals reach yields of 0.3% and 3%, respectively.[24, 25] Considerable efforts have been made to enhance the UCL intensity of UCNPs. Strategies include the application of inert or active shells in core–multi-shell structures to shield against surface quenching.[26-29] Furthermore, by capitalising on the discrete absorption and emission centres within UCNPs—namely sensitisers and activators—UCL performance can be improved through increased dopant concentrations.[30] Such modifications may also yield desirable features such as single-band emission and tunable UCL lifetimes.[31, 32] Nevertheless, excessive activator concentration can result in detrimental cross-relaxation (CR), while over-doping of sensitisers exacerbates energy back-transfer (EBT) from activators to sensitisers, as well as energy migration (EM) to internal defects or surface quenchers (SQs), all of which lead to significant energy loss.[33] To mitigate these effects and improve the UCL performance of highly doped UCNPs, various approaches have been developed, such as engineering dopant concentration distribution, exploiting beneficial CR, cell manipulation and interfacial energy transfer mediated by Tb^{3+} ions.[34, 35] Inorganic fluorides, owing to their low phonon energy and high chemical stability, are frequently adopted as host materials for RE doping.[36] Among these, hexagonal-phase $NaREF_4$ UCNPs exhibit lower symmetry and superior UCL performance compared to their tetragonal counterparts.[37, 38]

As UCL activators, Ho^{3+} ions also possess a high effective magnetic moment and short electronic relaxation time,[39, 40] making $NaHoF_4$ UCNPs ideal candidates for photo-induced therapy in addition to Ho-based computed tomography and high-field magnetic resonance imaging. However, studies on UCL from $NaHoF_4$ UCNPs remain limited, primarily due to severe concentration quenching induced by CR and SQs at the ultra-high Ho^{3+} doping levels required. Nonetheless, preliminary UCL fine-tuning and mechanistic exploration have been achieved by our

group and others using Ho@Yb UCNPs—specialised core–multi-shell structures in which activators are heavily doped in the core and inner shells, and sensitisers in the outer shells (e.g. $NaHoF_4$@$NaHoF_4$@$NaGdF_4$:60%Yb^{3+}). These structures have sometimes demonstrated UCL performance exceeding that of traditionally low-doped UCNPs, particularly through enhanced and purified red UCL, which is advantageous for imaging applications.[41] More in-depth theoretical studies are warranted to develop more efficient and flexible strategies for fine-tuning Ho-based UCL in $NaHoF_4$ UCNPs, thereby enhancing the application potential of this material.

Ho@Yb structures allow for doping configurations that are difficult or impossible to achieve in conventional low-doped and co-doped systems, offering valuable insights into UCL theory. In our previous work,[42] Zn^{2+} ions were introduced into single or multiple layers to uncover, for the first time, their distinct lattice distortion effects on the sensitising ability of Yb^{3+} and the luminescent properties of Ho^{3+}. The optimal Zn^{2+} doping concentrations were found to be 20 mol% for Ho^{3+} and 5 mol% for Yb^{3+}—a marked deviation from the commonly accepted value of 10 mol% for co-doping. In addition, Ce^{3+} doping has been extensively used to suppress non-radiative relaxation (NR) of Ho^{3+} ions and replace Ho^{3+}–Ho^{3+} CR with more favourable Ho^{3+}–Ce^{3+} CR, thereby enhancing red Ho-based emission.[43-45] In Ho@Yb structures, the previously puzzling decrease in total UCL intensity following Ce^{3+} doping can be reasonably explained by phonon energy shortage.[17] Notably, co-doping of Ce^{3+} with either Ho^{3+} or Yb^{3+} led to marked different UCL outcomes. Ce^{3+} ions doped into the shell exhibited interactions with surface groups that alleviated phonon energy shortage, facilitated Ho^{3+}–Ce^{3+} CR and mitigated surface quenching, compared to core-doped Ce^{3+}, which led to greater UCL intensity losses. These findings underscore the immense value of Ho@Yb structures for advancing UCL theory.

Building on our previous studies, we further investigated influencing factors that remain underexplored or are difficult to realise in traditional low- and co-doped systems, particularly with respect to Ce^{3+}-modulated UCL. A series of double- and triple-shell Ho@Yb UCNPs, with and without Ce^{3+} doping, were synthesised using the oleate method. The effects of varying Ho^{3+} concentration in the core and first shell, Yb^{3+} concentration in the second and third layers, and the number of shell layers were systematically evaluated. The analysis included UCL intensity, green-to-red (G/R) intensity ratios, decay lifetimes and G/R variation with pump power. Comprehensive mechanisms were revealed, encompassing phonon energy, CR, NR, ET, EBT, EM and surface quenching. Additionally, Ce^{3+} ions were doped selectively into the core, first shell, second shell or multiple layers to probe their positional influence. The colour tunability of Ce^{3+}-doped UCNPs under variable pump power was also assessed. This work contributes to a deeper understanding of highly doped UCNPs and Ce^{3+} doping strategies while enriching UCL fine-tuning methodologies and broadening the multifunctional application potential of $NaHoF_4$-based nanomaterials for photo-induced therapy and anti-counterfeiting technologies.

Results and discussion

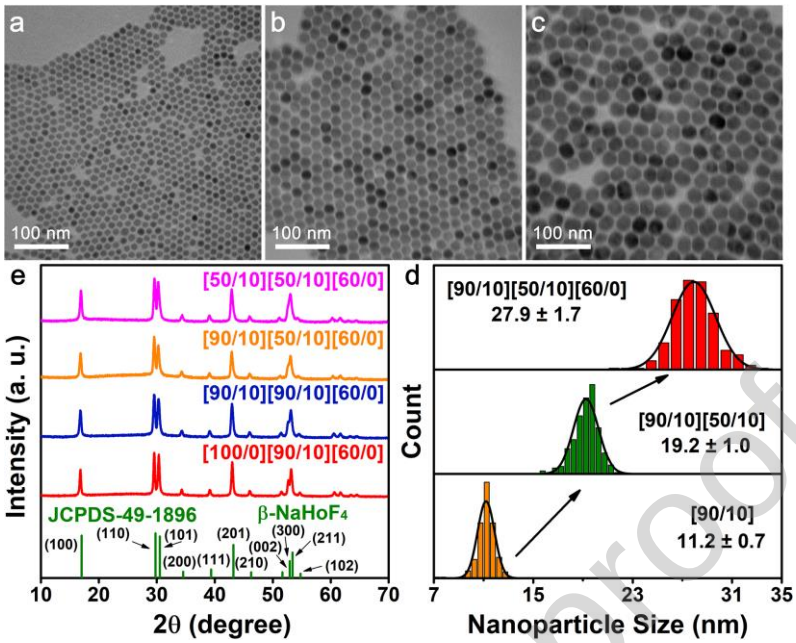

Figure 1. (a)–(d) TEM images and size distribution diagram of [90/10] ($NaHoF_4$:10%Ce^{3+}), [90/10][50/10] ($NaHoF_4$:10%Ce^{3+}@$NaHoF_4$:10%Ce^{3+},40%Gd^{3+}), and [90/10][50/10][60/0] ($NaHoF_4$:10%Ce^{3+}@$NaHoF_4$:10%Ce^{3+},40%Gd^{3+}@$NaGdF_4$:60%Yb^{3+}) UCNPs. The scale bars are 100 nm. (e) XRD patterns of different CSS UCNPs.

A series of core–shell–shell (CSS) $NaHoF_4$:Ce^{3+},Gd^{3+}@$NaHoF_4$:Ce^{3+},Gd^{3+}@$NaGdF_4$:Yb^{3+} UCNPs, hereafter denoted as [x_1/y_1][x_2/y_2][z/y_3] UCNPs (where x, y and z represent the concentrations of Ho^{3+}, Ce^{3+} and Yb^{3+} ions in each respective layer), were synthesised via the oleate-assisted method. In our design, high concentrations of the activator Ho^{3+} and the sensitiser Yb^{3+} were separately doped into the core and shells, forming Ho@Yb-featured structures. This concentration not only enabled high dopant concentrations but also allowed the creation of spatial concentrations that were difficult or impossible to achieve in traditional low-doping UCNPs. The concentration of outermost Yb^{3+} ions was fixed at 60 mol%, based on our prior findings,[46] while Ho^{3+} concentration in the core and first shell was modulated using Gd^{3+} ions. The evolution in size and morphology of the as-prepared CSS UCNPs is shown in **Fig. 1a–d** and **S1**. Spherical nanoparticles with mono-dispersity and high uniformity were successfully obtained. The average diameters of core, core–shell and CSS UCNPs were approximately 11, 18 and 27 nm, respectively, indicating inner shell $NaHoF_4$:Ce^{3+},Gd^{3+} and outer shell $NaGdF_4$:60%Yb^{3+} thickness of approximately 4 and 5 nm, respectively. XRD patterns (**Fig. 1e** and **S2**) confirmed the samples exhibited pure hexagonal phases, with diffraction peaks consistent with the standard β-$NaHoF_4$ (JCPDS-49-1896), providing a solid foundation for subsequent analyses.

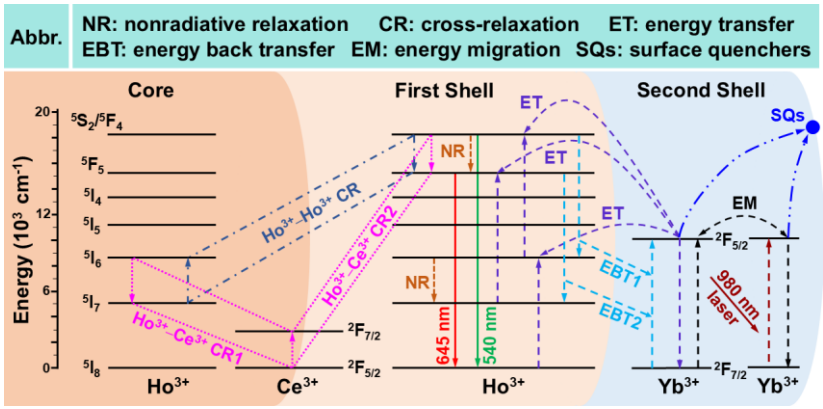

Figure 2. Energy diagrams and mechanisms of Ce^{3+}-doped Ho@Yb UCNPs.

To facilitate a more thorough discussion of the UCL properties of our samples, the typical energy processes and UCL features of Ho@Yb structures should be introduced. The relevant energy level diagrams and possible upconversion mechanism under Yb^{3+}/Ho^{3+} co-doping are shown in **Fig. 2**. Initially, sensitiser Yb^{3+} ions absorb 980-nm photons via ground-state absorption, promoting electrons from the ground state ($^2F_{7/2}$) to the excited state ($^2F_{5/2}$). Subsequently, the $^5I_6$ and $^5S_2/^5F_4$ states of Ho^{3+} ions are sequentially populated through ET from Yb^{3+} to Ho^{3+}, leading to green emission attributed to the $^5S_2/^5F_4 \rightarrow {}^5I_8$ transition. Red emission originates from the $^5F_5 \rightarrow {}^5I_8$ transition. There are generally two pathways by which the $^5F_5$ state of Ho^{3+} can be populated: (1) the $^5S_2/^5F_4 \rightarrow {}^5I_8$ transition via non-radiative relaxation (NR) from the $^5S_2/^5F_4$ state, or Ho^{3+}–Ho^{3+} CR via $^5F_4/^5S_2$ (Ho_1^{3+}) + $^5I_7$ (Ho_2^{3+}) → $^5F_5$ (Ho_1^{3+}) + $^5I_6$ (Ho_2^{3+}); (2) NR from $^5I_6 \rightarrow {}^5I_7$, followed by Yb^{3+}–Ho^{3+} ET from $^5I_7 \rightarrow {}^5F_5$. Both routes are typically inefficient in conventional low-doped $NaREF_4$ UCNPs, resulting in green-dominated UCL.[47-50] To enhance the intensity and spectral purity of Ho-based red UCL, Ce^{3+} doping is a widely adopted strategy.[51-54] Ce^{3+} ions facilitate CR with Ho^{3+} through two main processes: CR1 of $^5I_6$ (Ho^{3+}) + $^2F_{5/2}$ (Ce^{3+}) → $^5I_7$ (Ho^{3+}) + $^2F_{7/2}$ (Ce^{3+}) and CR2 of $^5S_2/^5F_4$ (Ho^{3+}) + $^2F_{5/2}$ (Ce^{3+}) → $^5F_5$ (Ho^{3+}) + $^2F_{7/2}$ (Ce^{3+}). These processes significantly reduce I_G and enhance I_R, with CR1 generally being more efficient than CR2.[55-57]

Compared to low-doped UCNPs, highly doped Ho@Yb systems exhibit additional characteristic energy processes, including Ho^{3+}–Yb^{3+} EBT, such as $^5F_4/^5S_2$ (Ho^{3+}) + $^2F_{7/2}$ (Yb^{3+}) → $^5I_6$ (Ho^{3+}) + $^2F_{5/2}$ (Yb^{3+}) and $^5F_5$ (Ho^{3+}) + $^2F_{7/2}$ (Yb^{3+}) → $^5I_7$ (Ho^{3+}) + $^2F_{5/2}$ (Yb^{3+}); Yb^{3+}–Yb^{3+} EM: $^2F_{5/2}$ (Yb_1^{3+}) + $^2F_{7/2}$ (Yb_2^{3+}) → $^2F_{7/2}$ (Yb_1^{3+}) + $^2F_{5/2}$ (Yb_2^{3+}); frequent Ho^{3+}–Ho^{3+} CR; and severe energy quenching via SQs. These mechanisms collectively lead to a significant decrease in UCL intensity, as represented by processes such as EBT–SQ, EM–SQ, EBT–EM–…–EM–ET (EBT–EM–ET for short) and EBT–EM–…–EM–SQ (EBT–EM–SQ) in **Fig. 2**. Furthermore, Ho@Yb UCNPs exhibit unique UCL properties. First, only Ho^{3+} ions within a distance *d* away from the active shell can contribute effectively to UCL, with *d* varying based on doping concentration and nanoparticle structure. Second, Ho^{3+} ions near the active shell tend to favour green emission intensity (I_G), while those further away red emission intensity (I_R). Third, larger $NaHoF_4$ core sizes are beneficial for enhanced I_R. Lastly, the optimal number of active shell layers depends on core size and the distributions of Yb^{3+} within the shells. In general, two- or three-layer shell structures with a decreasing Yb^{3+} concentration gradient from inner to outer shell tend to exhibit optimal UCL performance.

In our previous study,[17] we demonstrated that Ce^{3+}-doped Ho@Yb UCNPs can modulate UCL behaviour depending on concentration and location of Ce^{3+}. Specifically, introducing 10 mol% Ce^{3+}

into the $NaHoF_4$:Gd^{3+} core significantly reduced UCL intensity due to competition over phonon energy between the $^2F_{7/2} \rightarrow {}^2F_{5/2}$ transitions of Ce^{3+} ions and the phonon-mediated UCL processes, including Ho^{3+}–Ho^{3+} CR, NR of Ho^{3+} ions and Yb^{3+}–Ho^{3+} phonon-assisted ET, as shown in **Fig. 2**. In contrast, Ce^{3+} ions doped into the $NaGdF_4$:Yb^{3+} active shells can interact with surface groups to mitigate phonon energy limitations, thereby preserving the efficiency of Ho^{3+}–Ce^{3+} CR. Additionally, core-doped Ce^{3+} may disrupt the UCL characteristics of Ho@Yb UCNPs and suppress I_R. However, this influence is not considered significant in the present study for several reasons. First, the $NaHoF_4$ cores used here (~18 nm) are considerably larger than those in our previous work (~6.5 nm), resulting in distinct phonon energy conditions. Second, in the earlier study, only regions surrounding Ce^{3+} ions were I_R-favoured under 10 mol% doping, whereas in large cores with similar shell thicknesses, the intrinsic tendencies of Ho^{3+} for I_G and I_R are more pronounced and less susceptible to alteration. Third, the overall particle sizes in the CSS samples are significantly larger, implying greater phonon energy and reduced sensitivity to phonon-related effects. Consequently, Ho^{3+}–Ho^{3+} CR becomes more efficient and increasingly significant, potentially leading to different UCL behaviours in this system.

Subsequently, the UCL spectra of the aforementioned Ce^{3+}-doped CSS UCNPs, under continuous 980-nm NIR laser excitation, are shown in **Fig. 3a**. The green emission band peaked at ~540 nm, while the red emission band peaked at ~645 nm. Both emissions were identified as two-phonon processes (**Fig. S3**). The influences from ion diffusion between layers on UCL of Ho@Yb UCNPs have been proved insignificant in our previous researches.[31, 46] To better visualise the behaviour of I_G, I_R, total emission intensity (I_{Total}) and green-to-red intensity (G/R) ratio, their respective variation trends were plotted in **Fig. 3b**. First, when compared with [100/0][90/10][60/0] UCNPs, the [90/10][90/10][60/0] samples—containing additional Ce^{3+} ions in the core—exhibited a slight decrease in both I_G and I_R. This result aligns with our previous findings, indicating that excessive core-doped Ce^{3+} ions can exacerbate phonon energy shortages and ultimately reduce the efficiency of Ho^{3+}–Ce^{3+} CR. Second, the spatial concentration distribution of activators was tuned by substituting Ho^{3+} with Gd^{3+} in the core and first shell (S_1). In [90/10][50/10][60/0] UCNPs, reducing Ho^{3+} concentration in S_1 from 90 to 50 mol% resulted in a slight increase in both I_G and I_R. Upon further reduction of Ho^{3+} content in the core, the [50/10][50/10][60/0] UCNPs displayed a continued increase in I_G, accompanied by a reduction in I_R. These observations suggest that the spatial distribution of Ho^{3+} affects the red-tuning effect of Ce^{3+} ions.

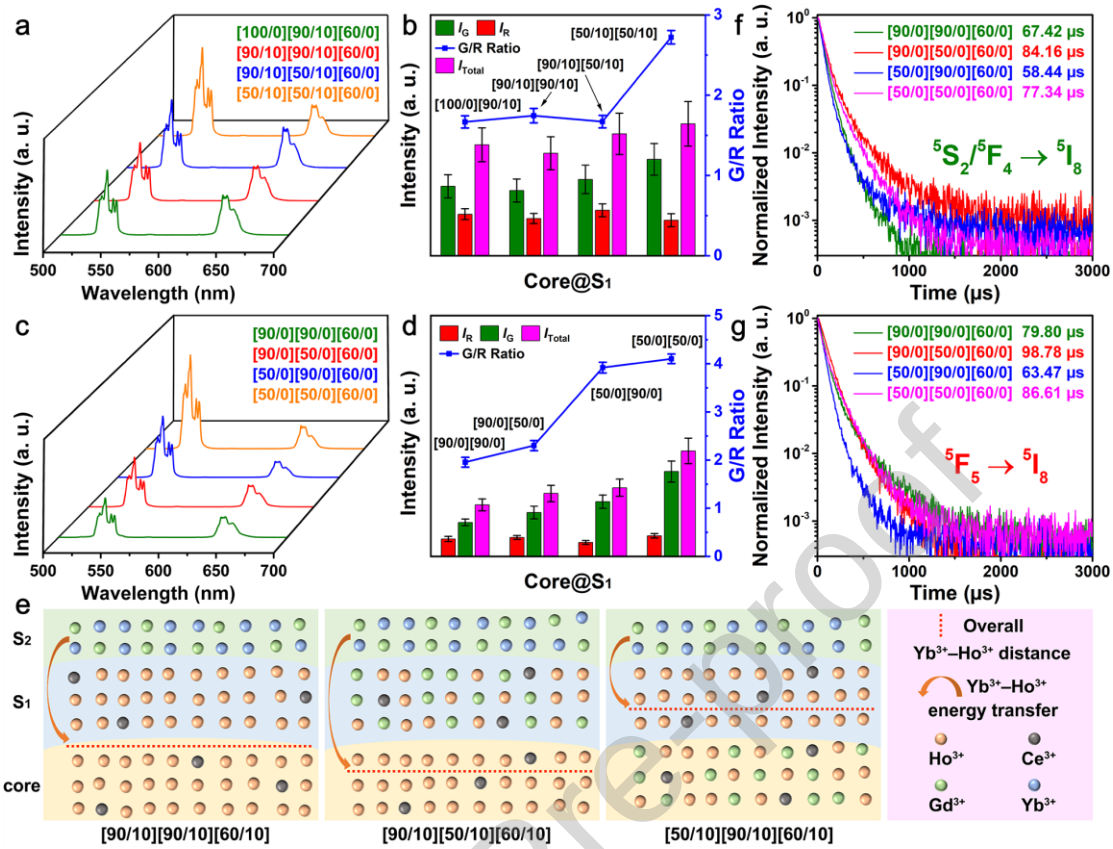

Figure 3. (a)–(b) UCL spectra and properties of Ce^{3+}-doped CSS [100/0][90/10][60/0] ($NaHoF_4$@$NaHoF_4$:10%Ce^{3+}@$NaGdF_4$:60%Yb^{3+}), [90/10][90/10][60/0] ($NaHoF_4$:10%Ce^{3+}@$NaHoF_4$:10%Ce^{3+}@$NaGdF_4$:60%Yb^{3+}), [90/10][50/10][60/0] ($NaHoF_4$:10%Ce^{3+}@$NaHoF_4$:10%Ce^{3+},40%Gd^{3+}@$NaGdF_4$:60%Yb^{3+}) and [50/10][50/10][60/0] ($NaHoF_4$:10%Ce^{3+},40%Gd^{3+}@$NaHoF_4$:10%Ce^{3+},40%Gd^{3+}@$NaGdF_4$:60%Yb^{3+}) UCNPs. (c)–(d) UCL spectra and properties of Ce^{3+}-free CSS [90/0][90/0][60/0] ($NaHoF_4$:10%Gd^{3+}@$NaHoF_4$:10%Gd^{3+}@$NaGdF_4$:60%Yb^{3+}), [90/0][50/0][60/0] ($NaHoF_4$:10%Gd^{3+}@$NaHoF_4$:50%Gd^{3+}@$NaGdF_4$:60%Yb^{3+}), [50/0][90/0][60/0] ($NaHoF_4$:50%Gd^{3+}@$NaHoF_4$:10%Gd^{3+}@$NaGdF_4$:60%Yb^{3+}) and [50/0][50/0][60/0] ($NaHoF_4$:50%Gd^{3+}@$NaHoF_4$:50%Gd^{3+}@$NaGdF_4$:60%Yb^{3+}) UCNPs. (e) Schematic illustrations of overall Yb^{3+}–Ho^{3+} distance variations with Ho^{3+} concentration distributions in core and S_1. (f)–(g) Decay curves of green UCL at 540 nm and red UCL at 645nm of UCNPs in (c).

To further investigate these results, a series of Ce^{3+}-free CSS UCNPs were synthesised with varying Ho^{3+} concentration distributions. The synthesised hexagonal-phase samples were uniform and displayed average sizes comparable to the Ce^{3+}-doped CSS UCNPs (**Fig. S4**). Their UCL spectra and corresponding property variations are illustrated in **Fig. 3c–d**. With the progressive reduction of Ho^{3+} concentration in S_1, the core and both regions, I_G and G/R ratios consistently increased, while I_R exhibited an unobvious trend (see **Note S1** in **SI**). The increase in I_G with decreasing Ho^{3+} concentration confirms the dominant role of Ho^{3+}–Ho^{3+} CR in reducing the G/R ratio in Ce^{3+}-free UCNPs. Notably, the I_G of [50/0][90/0][60/0] and [50/0][50/0][60/0] UCNPs was significantly higher than of the other samples. This suggests that in Ho@Yb UCNPs, Ho^{3+} ions beyond *d* also influence UCL behaviour via Ho^{3+}–Ho^{3+} CR. In other words, Ho^{3+} ions located within *d* contribute both to emission and CR, while those beyond *d* mainly participate in CR. A Förster resonance ET theory applies to sensitiser–activator ET in UCL processes,[30, 58] and given that Yb^{3+}

can sensitise Ho^{3+} ions at even 10.7 nm,[31] so all Ho^{3+} ions in the core and S_1 are considered effective participants. Another notable observation is that I_R increased as the Ho^{3+} concentration in S_1 decreased. This effect results from a competitive interplay between Ho^{3+}–Ho^{3+} CR and energy loss mechanisms such as SQs and EBT. Although reducing the Ho^{3+} content in S_1 to 50 mol% slightly lowered CR efficiency and increased the overall Yb^{3+}–Ho^{3+} distance, it also allowed Yb^{3+} ions to sensitise a greater portion of Ho^{3+} ions situated deeper within S_1 and the core. This occurred due to the reduced number of immediate energy acceptors within the original *d* (**Fig. 3e**). Consequently, the overall distance between activated Ho^{3+} ions and SQs or ground-state Yb^{3+} ions increased, as did the value of *d*, which is positively correlated (see **Note S2** in **SI**). These changes reduced the likelihood of negative processes (e.g. surface energy quenching, EBT, EBT–SQ and EBT–EM–SQ; see **Fig. 2**), thereby enhancing I_R. This analysis is consistent with the single-exponential decay times (τ) fitted for Ce^{3+}-free UCNPs. Both green (540 nm) and red (645 nm) UCL decay times were longer for [90/0][50/0][60/0] and [50/0][50/0][60/0] UCNPs (**Fig. 3f–g**), indicating reduced energy loss from Ho^{3+} ions in the $^5S_2/^5F_4$ and $^5F_5$ states. In conclusion, for the synthesised CSS UCNPs with an S_1 composition of [60/0], Ho^{3+} ions in both the core and S_1 contributed to Ho^{3+}–Ho^{3+} CR. Reducing the Ho^{3+} concentration in S_1 proved beneficial for improving UCL intensity and extending τ.

Returning to the CSS UCNPs doped with Ce^{3+} in both the core and S_1, a reduction in Ho^{3+} content did result in decreased Ho^{3+}–Ho^{3+} CR. However, the tendency towards I_R did not diminish accordingly, as the Ho^{3+}–Ce^{3+} CR was enhanced due to the alleviation of phonon energy shortage, as demonstrated in [90/10][90/10][60/0] and [90/10][50/10][60/0] UCNPs (**Fig. 3b**). Nonetheless, the [50/10][50/10][60/0] samples exhibited a higher G/R ratio than the [90/10][50/10][60/0] samples. This phenomenon can be attributed to *d* variations. As previously discussed, reducing the Ho^{3+} concentration in S_1 led to an expansion of *d*. Conversely, reducing Ho^{3+} in the core left fewer Ho^{3+} ions available for activation within the core region, thereby increasing the probability of Yb^{3+}–Ho^{3+} ET to Ho^{3+} ions in S_1. In other words, *d* contracted (**Fig. 3e**), as relatively more Ho^{3+} ions contributing to emission were located closer to the interface between the second shell (S_2) and S_1 (**Fig. S5** in **SI**). Ho^{3+} ions situated near the S_1/S_2 interface were more easily sensitised directly into the $^5S_2/^5F_4$ state, contributing to green emission. Meanwhile, Ce^{3+} ions in the core were too distant from these Ho^{3+} ions to support efficient Ho^{3+}–Ce^{3+} CR. As a result, the G/R ratio increased despite the enhancement of Ho^{3+}–Ce^{3+} CR from core-doped Ce^{3+} ions. The fact that [50/10][50/10][60/0] UCNPs exhibited a larger *d* yet significantly higher G/R ratio than [90/10][90/10][60/0] ones indicates that the improvement in Ho^{3+}–Ce^{3+} CR due to reduced phonon energy shortage was insufficient to counteract the decline in Ho^{3+}–Ho^{3+} CR caused by reduced Ho^{3+} concentration in both core and S_1. The limitations of Ce^{3+} doping confined only to the core and S_1 will be further analysed later. In brief, for CSS UCNPs with Ce^{3+} in both core and S_1, reducing Ho^{3+} concentration in S_1 alone favoured longer τ values, while reducing Ho^{3+} in both core and S_1 had the opposite effect and was not optimal for achieving strong red Ho-based UCL.

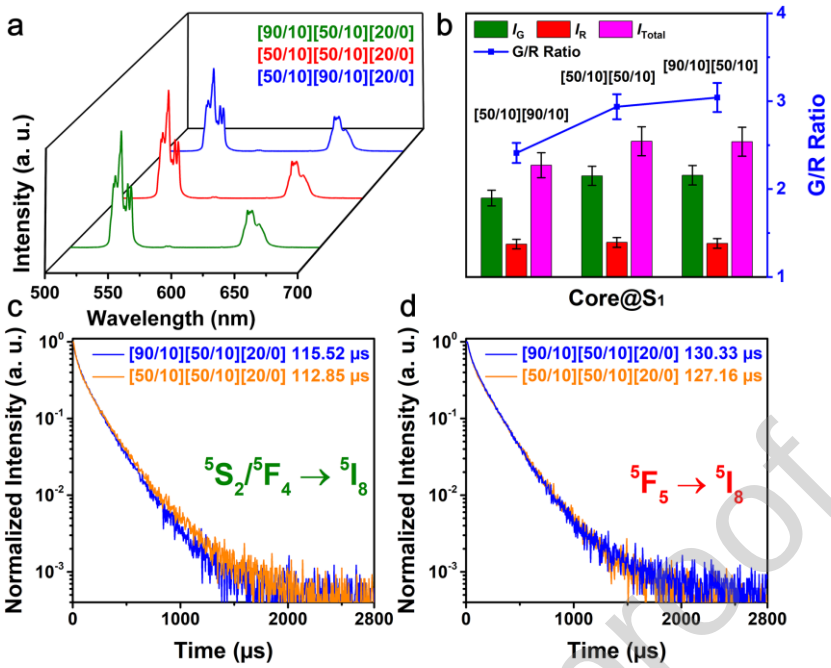

Figure 4. (a)–(b) UCL spectra and properties of Ce^{3+}-doped CSS [90/10][50/10][20/0] ($NaHoF_4$:10%Ce^{3+}@$NaHoF_4$:10%Ce^{3+},40%Gd^{3+}@$NaGdF_4$:20%Yb^{3+}), [50/10][50/10][20/0] ($NaHoF_4$:10%Ce^{3+},40%Gd^{3+}@$NaHoF_4$:10%Ce^{3+},40%Gd^{3+}@$NaGdF_4$:20%Yb^{3+}) and [50/10][90/10][20/0] ($NaHoF_4$:10%Ce^{3+},40%Gd^{3+}@$NaHoF_4$:10%Ce^{3+}@$NaGdF_4$:20%Yb^{3+}) UCNPs. (c)–(d) Decay curves of green UCL at 540 nm and red UCL at 645 nm of [90/10][50/10][20/0] and [50/10][50/10][20/0] UCNPs.

To gain further insight, Ce^{3+}-doped CSS UCNPs with an S_2 composition of [20/0] were synthesised. As shown in **Figs. S6–7** (also see **Note S3** in **SI**), the [50/10][90/10][20/0], [90/10][50/10][20/0] and [50/10][50/10][20/0] UCNPs exhibited a pure hexagonal phase and possessed core sizes and shell thicknesses comparable to the previous samples. Their UCL spectra and corresponding properties are presented in **Fig. 4a–b**. Notably, I_R remained nearly constant across these samples, while I_G varied primarily with the composition of S_1. This suggests that an S_2 composition of [20/0] was insufficient to provide the extent of ET observed in [60/0] and could not adequately sensitise Ho^{3+} ions in the core to drive effective Ho^{3+}–Ho^{3+} CR. As such, the core regions of these samples can be reasonably excluded from the analysis of their UCL properties. Given that emission was predominantly from surface Ho^{3+} ions, which are generally inclined towards I_G, little variation in I_R was expected. However, both I_G and G/R ratio increased from [50/10][90/10][20/0] to [50/10][50/10][20/0] UCNPs. This result suggests that, in the absence of significant phonon energy consumption due to ET and CR, reducing Ho^{3+} concentration may not significantly enhance Ho^{3+}–Ce^{3+} CR via phonon energy alleviation. Instead, the overall efficiency of both Ce^{3+}–Ho^{3+} and Ho^{3+}–Ho^{3+} CR decreased. Interestingly, with Ce^{3+} doping, I_{Total}, particularly I_G, was even higher in UCNPs with S_2 = [20/0] than with [60/0] (**Fig. S8**). This could be attributed to the following factors: (1) the reduced Yb^{3+} concentrations (20 mol%) resulted in less phonon energy consumption during ET, (2) the S_2 thickness (~5 nm) remained sufficient to supply a moderate level of sensitisation to Ho^{3+} emitters and (3) most importantly, EBT and surface energy quenching were significantly suppressed due to enhanced Gd^{3+}-based energy shielding. This interpretation is supported by the decay curves for [90/10][50/10][20/0] and [50/10][50/10][20/0] UCNPs (**Fig. 4c–d**). The τ values for both I_G and I_R showed no significant variation following the reduction in Ho^{3+} concentration in the core, indicating that the overall distance between activated Ho^{3+} ions and the nanoparticle

surface remains largely unaffected. Furthermore, all τ values were notably higher than those for UCNPs with S_2 = [60/0], confirming reduced interference from EBT, SQs and phonon energy shortage. In summary, the distribution of Yb^{3+} ions plays a critical role in fine-tuning UCL properties and should be carefully considered when designing Ce^{3+}-doped UCNPs. For CSS structures, an S_2 composition of [20/0] was found to be less favourable for achieving high-purity red UCL.

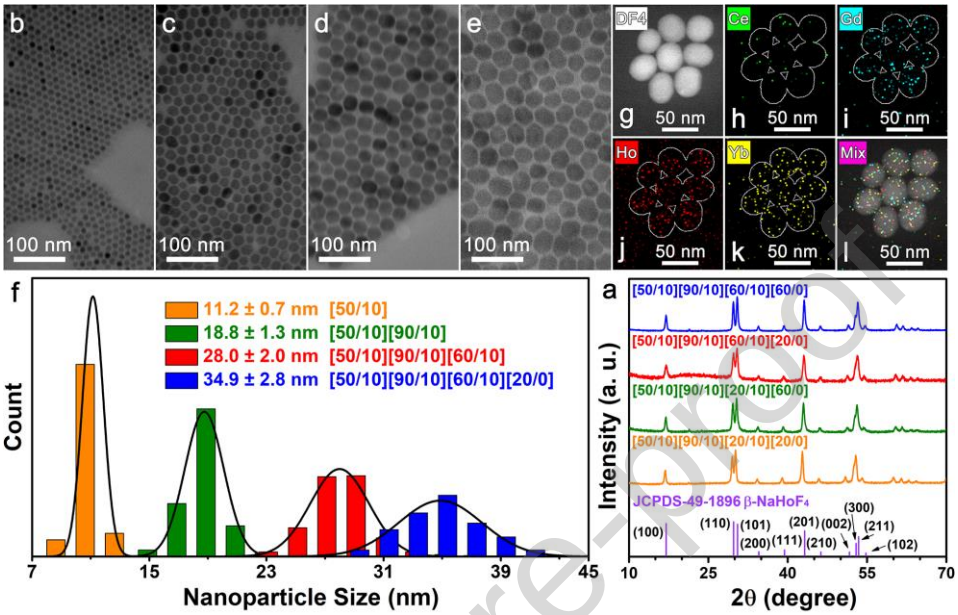

Figure 5. (a) XRD patterns of selected CSSS UCNPs. (b)–(f) TEM images and size distribution diagram of [50/10] ($NaHoF_4$:10%Ce^{3+},40%Gd^{3+}), [50/10][90/10] ($NaHoF_4$:10%Ce^{3+},40%Gd^{3+}@$NaHoF_4$:10%Ce^{3+}), [90/10][50/10][60/10] ($NaHoF_4$:10%Ce^{3+},40%Gd^{3+}@$NaHoF_4$:10%Ce^{3+}@$NaGdF_4$:60%Yb^{3+},10%Ce^{3+}) and [90/10][50/10][60/10][20/0] ($NaHoF_4$:10%Ce^{3+},40%Gd^{3+}@$NaHoF_4$:10%Ce^{3+}@$NaGdF_4$:60%Yb^{3+},10%Ce^{3+}@$NaGdF_4$:20%Yb^{3+}) UCNPs. The scale bars are 100 nm. (g)–(l) Elemental mapping images of [50/10][90/10][20/10][60/0] UCNPs. The scale bars are 50 nm. For better presentation, the margins of the UCNPs in (g) were outlined with white curves in (h)–(l).

Furthermore, core–shell–shell–shell (CSSS) $NaHoF_4$:Ce^{3+},Gd^{3+}@$NaHoF_4$:Ce^{3+},Gd^{3+}@$NaGdF_4$:Ce^{3+},Yb^{3+}@$NaGdF_4$:Yb^{3+} UCNPs (abbreviated in the same manner as CSS structures) were synthesised with varied Ho^{3+} and Yb^{3+} concentration distributions in the core and S_1, and in S_2 and S_3, respectively, to gain deeper insights. The ICP-MS characterizations showed actual concentration ratios in fine agreement with as-designed doping content and structures (see **Note S4** in **SI**). A constant 10 mol% of Ce^{3+} ions was doped into the core, S_1 and S_2 layers. All samples exhibited pure hexagonal-phase structures (**Fig. 5a** and **S9**). Their core sizes and the thicknesses of S_1 and S_2 matched those of the previously synthesised CSS UCNPs, while the thickness of S_3 was ~3.5 nm (**Fig. 5b–f** and **S10–12**). High-resolution TEM and elemental mapping images of [50/10][90/10][20/10][60/0] and [90/10][90/10][60/10][20/0] UCNPs are presented in **Fig. S13–14 and 5g–l**. Clear lattice fringes, along with elemental signals for Ho, Yb, Gd and Ce, were observed. In addition, Yb signals appeared relatively closer to the nanoparticle surfaces compared to those of Ho^{3+} (**Fig. 5j–k**), further confirming the successful synthesis of the intended multi-layer structures. **Table 1** provides an overview of the specific structures and associated reference numbers for all CSSS samples.

UCNPs 1–16 were categorised into four groups based on identical core and S_1 compositions but differing S_2 and S_3 contents. Their UCL spectra and intensity trends are illustrated in **Fig. 6a–b**.

In each group, I_G, I_R and I_{Total} in **Fig. 6b** followed similar patterns, with the lowest and highest values generally observed in samples with S_2@S_3 configurations of [20/10][60/0] and [60/10][20/0], respectively—except for the I_R of UCNPs 1 and I_G of UCNPs 11. It is well established that, in multi-shell structures, a Yb^{3+} concentration gradient decreasing from the inner to the outer shells ('>') optimally supports inward ET and provides effective surface energy shielding. In contrast, equal concentration throughout layers ('=') is moderately effective, and gradients increasing from inner to outer shells ('<') perform the worst.[46, 59] In '>' distributions, although EBT is more likely due to high local Yb^{3+} content near activators, outward Yb^{3+}–Yb^{3+} EM and surface quenching are significantly suppressed because of fewer external ground-state Yb^{3+} acceptors and enhanced surface shielding by inert Gd^{3+} dopants. Generally, detrimental energy processes such as EBT–SQ, EBT–EM–SQ and EBT–EM–ET occur with reduced frequency, allowing Ho^{3+} activators to maintain stronger radiative emissions. In such cases, EBT becomes a secondary concern when compared with the considerably enhanced inward ET. This conclusion is supported by τ for I_G and I_R across the groups (**Fig. 6c–d** and **Table 1**, also see **Note S5** in **SI**). UCNPs with '>' Yb^{3+} distributions consistently exhibited the second-longest τ values, significantly longer than those of samples with S_2@S_3 of [20/10][60/0] or [60/10][60/0], due to reduced EBT and surface energy quenching, though slightly shorter than or comparable to the τ values of UCNPs with S_2@S_3 of [20/10][20/0], where EBT was nearly eliminated. Notably, although both [60/10][60/0] and [20/10][20/0] represent '=' Yb^{3+} distributions, their sensitising efficiency differed significantly. The [20/10][20/0] configuration, containing only 20 mol% Yb^{3+}, was relatively inefficient in capturing 980 nm photons and mediating EM inward. Additionally, the distance from the particle surface to the nearest Ho^{3+} ions in S_1 (~8 nm) was too great to support efficient ET. Nevertheless, this design significantly limited EBT and surface quenching. As a result, a small number of Ho^{3+} ions were excited to the $^5S_2$/$^5F_4$ and $^5F_5$ states, but these favoured radiative over NR decay, leading to lower I_{Total} yet longer τ values than those of '>' distributed UCNPs. In contrast, the S_2@S_3 of [60/10][60/0] design offered increased Yb^{3+} availability for sensitisation and EM, yet also facilitated more severe EBT and surface quenching. Given that surface energy quenching is a critical factor limiting UCL performance, both I_{Total} and τ values were significantly reduced.

Table 1. Specific structures, given numbers, and decay times of green UCL at 540 nm and red UCL at 645 nm of different CSSS samples. In [x_1/y_1][x_2/y_2][z/y_3], x, y and z represent the concentrations of Ho^{3+}, Ce^{3+} and Yb^{3+} ions in each respective layer.

No.	Structures	Abbreviations	Decay times (μs)	
			540 nm	645 nm
1	Ho:10Ce@Ho:10Ce@Gd:20Yb,10Ce@Gd:20Yb	[90/10][90/10][20/10][20/0]	87.28	112.49
2	Ho:10Ce@Ho:10Ce@Gd:20Yb,10Ce@Gd:60Yb	[90/10][90/10][20/10][60/0]	68.69	86.09
3	Ho:10Ce@Ho:10Ce@Gd:60Yb,10Ce@Gd:20Yb	[90/10][90/10][60/10][20/0]	83.00	101.95
4	Ho:10Ce@Ho:10Ce@Gd:60Yb,10Ce@Gd:60Yb	[90/10][90/10][60/10][60/0]	60.16	70.96
5	Ho:10Ce@Ho:40Gd,10Ce@Gd:20Yb,10Ce@Gd:20Yb	[90/10][50/10][20/10][20/0]	142.51	192.65
6	Ho:10Ce@Ho:40Gd,10Ce@Gd:20Yb,10Ce@Gd:60Yb	[90/10][50/10][20/10][60/0]	76.57	111.19
7	Ho:10Ce@Ho:40Gd,10Ce@Gd:60Yb,10Ce@Gd:20Yb	[90/10][50/10][60/10][20/0]	134.95	167.15
8	Ho:10Ce@Ho:40Gd,10Ce@Gd:60Yb,10Ce@Gd:60Yb	[90/10][50/10][60/10][60/0]	67.07	93.25
9	Ho:40Gd,10Ce@Ho:10Ce@Gd:20Yb,10Ce@Gd:20Yb	[50/10][90/10][20/10][20/0]	130.51	144.41
10	Ho:40Gd,10Ce@Ho:10Ce@Gd:20Yb,10Ce@Gd:60Yb	[50/10][90/10][20/10][60/0]	63.65	72.51
11	Ho:40Gd,10Ce@Ho:10Ce@Gd:60Yb,10Ce@Gd:20Yb	[50/10][90/10][60/10][20/0]	123.23	164.97

12	Ho:40Gd,10Ce@Ho:10Ce@Gd:60Yb,10Ce@Gd:60Yb	[50/10][90/10][60/10][60/0]	46.76	60.03
13	Ho:40Gd,10Ce@Ho:40Gd,10Ce@Gd:20Yb,10Ce@Gd:20Yb	[50/10][50/10][20/10][20/0]	146.78	199.92
14	Ho:40Gd,10Ce@Ho:40Gd,10Ce@Gd:20Yb,10Ce@Gd:60Yb	[50/10][50/10][20/10][60/0]	63.15	88.54
15	Ho:40Gd,10Ce@Ho:40Gd,10Ce@Gd:60Yb,10Ce@Gd:20Yb	[50/10][50/10][60/10][20/0]	146.56	205.86
16	Ho:40Gd,10Ce@Ho:40Gd,10Ce@Gd:60Yb,10Ce@Gd:60Yb	[50/10][50/10][60/10][60/0]	53.07	72.39
17	Ho:50Gd@Ho:10Gd@Gd:60Yb,10Ce@Gd:20Yb	[50/0][90/0][60/10][20/0]	71.39	95.41
18	Ho:10Ce@Ho:10Gd@Gd:60Yb@Gd:20Yb	[90/10][90/0][60/0][20/0]	96.01	109.41
19	Ho:10Gd@Ho:10Ce@Gd:60Yb@Gd:20Yb	[90/0][90/10][60/0][20/0]	83.35	102.65

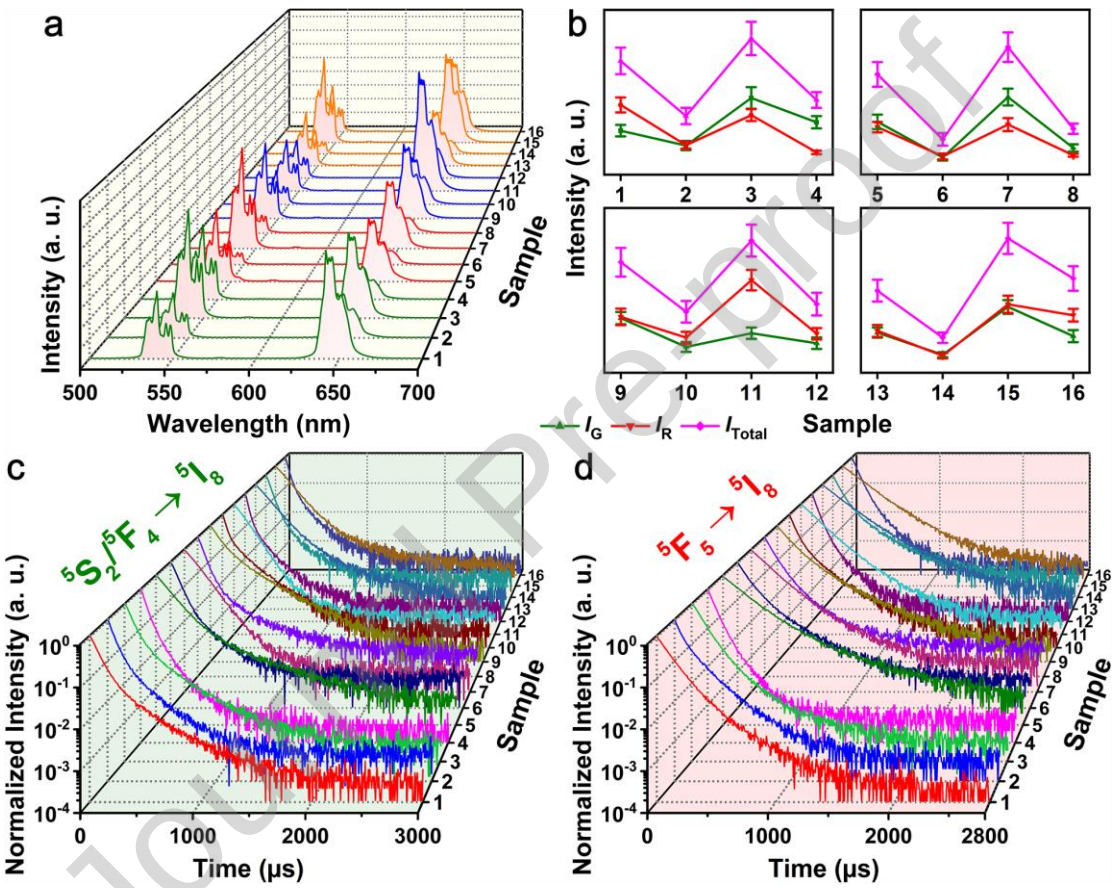

Figure 6. (a) UCL spectra, (b) UCL properties, (c) decay curves of green UCL at 540 nm, and (d) decay curves of red UCL at 645 nm of 1–16 UCNPs.

Furthermore, the influences from *d* variations and the phonon energy shortage derived from Yb^{3+} concentration distributions in S_2 and S_3 should be considered for a more comprehensive study. As mentioned earlier, the parameter *d* varied with the doping concentrations and nanoparticle structures of Ho@Yb UCNPs. Specifically, the more efficient sensitising energy supply towards the interior and the more surface energy protection that was provided, the greater the length of *d*.[31, 46] As such, S_2@S_3 of [60/10][20/0] exhibited the largest *d*, while [20/10][60/0] showed the smallest. When *d* increased in Ho@Yb UCNPs, more Ho^{3+} ions in the interior were activated for emission, and these ions were farther from surface Yb^{3+} ions, which reduced the negative effect of EBT and surface energy quenching. Although Ho^{3+} ions in the interior benefitted I_R, more phonon energy was consumed by phonon-related processes, such as NR of Ho^{3+} ions, Ho^{3+}–Ho^{3+} CR and phonon-assisted Yb^{3+}–Ho^{3+} ET. With Ce^{3+} doping in both the core and S_1 layer, facilitating more efficient

Ho^{3+}–Ce^{3+} CR compared to Ho^{3+}–Ho^{3+}, this consumption became significant, leading to a phonon energy shortage that hindered both CR and UCL efficiency. Because UCNPs 1–4 had the highest Ho^{3+} concentration in the core and S_1, the phonon energy shortage was most severe when *d* was increased by S_2@S_3 of [60/10][20/0]. The Ho^{3+}–Ce^{3+} and Ho^{3+}–Ho^{3+} CR processes relatively did not function efficiently, resulting in a higher G/R ratio. In contrast, S_2@S_3 of [20/10][20/0] in UCNPs 1 reduced the phonon energy shortage due to a relatively shorter *d* and, importantly, further mitigated energy loss due to EBT and surface energy quenching. The efficiency of both Ho^{3+}–Ce^{3+} and Ho^{3+}–Ho^{3+} CR was not as greatly reduced, allowing Ho^{3+} ions to remain longer in the $^5S_2/^5F_4$ and $^5F_5$ states, providing more opportunities for CR, thus resulting in the lowest G/R ratio among UCNPs 1–4, as shown in **Fig. 6b**. The exception for the I_R in UCNPs 1 was explained, and proposed mechanisms for the I_G of UCNPs 11 are discussed later. Additionally, the reduction in Ho^{3+} concentration in both the core and S_1 led to a higher I_{Total} enhancement rate of 63.71% from S_2@S_3 of [20/10][20/0] to [60/10][20/0], compared to 19.75%, 27.27% and 19.64% for the other Ho^{3+} concentration distributions, as seen in **Fig. 6b**. This enhancement was attributed to the relatively alleviated phonon energy shortage, primarily resulting from less Ho^{3+}–Ho^{3+} CR. In summary, Yb^{3+} concentration distributions can fine-tune UCL properties mainly by affecting sensitising energy transfer, surface energy protection and Ce^{3+}-induced phonon energy shortage. '>'-distributed CSSS UCNPs exhibited the highest I_{Total}.

UCNPs 1–16 were then divided into another four groups, with S_2 and S_3 being identical but differing in core and S_1, to investigate the influences of variations in Ho^{3+} concentration distribution. Line charts of I_G, I_R, I_{Total} and G/R ratios for UCNPs 1–16 were collected in **Fig. 7a–d** and **S15**.

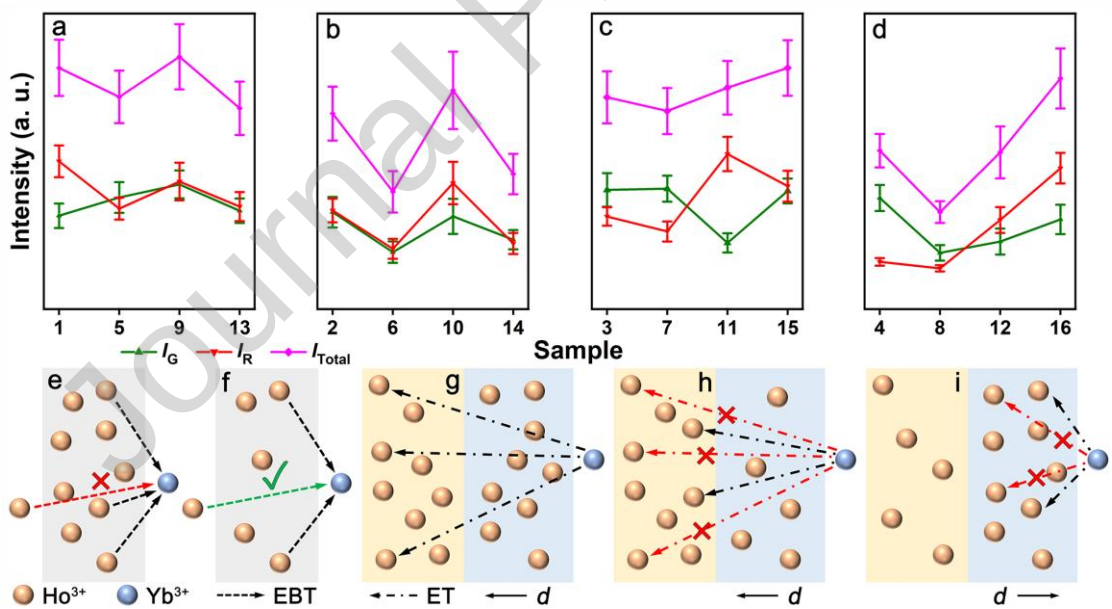

Figure 7. (a)–(d) Line charts of variations of I_G, I_R and I_{Total} for groups of 1/5/9/13, 2/6/10/14, 3/7/11/15 and 4/8/12/16 UCNPs, respectively. (e)–(f) Schematic graphs of shelter of surrounding activated Ho^{3+} ions. (g)–(i) Schematic comparisons of variations of *d* and Yb^{3+}–Ho^{3+} ET by S_2@S_3 of [60/10][20/0], core@S_1 of [90/10][50/10], and core@S_1 of [50/10][90/10], respectively.

Compared with the groups in **Fig. 6b**, the I_{Total} values exhibited different trends. For UCNPs with S_2 of [20/10], a reduction in Ho^{3+} solely in the core led to the highest I_{Total}, whereas for S_2 of [60/10], a reduction in Ho^{3+} concentration in both the core and S_1 had the same effect. This phenomenon can be explained by the combined influences of *d* and the phonon energy shortage. As

noted earlier for CSS UCNPs, both Ho^{3+} ions in the core and S_1 were activated and contributed to the UCL-related processes; *d* was modulated by the Ho^{3+} concentration distributions in the core@S_1, and the sequence of values should be [50/10][90/10] < [90/10][90/10] < [50/10][50/10] < [90/10][50/10] under the same Yb^{3+} sensitising conditions. Thus, UCNPs 9 and 10 exhibited the shortest *d* in their respective groups. As the sensitising energy supply from S_2@S_3 of neither [20/10][20/0] nor [20/10][60/0] was efficient, and S_2 of [20/10] resulted in less EBT, a shorter distance between Yb^{3+} and Ho^{3+} ions improved Yb^{3+}–Ho^{3+} ET efficiency, enhancing I_{Total}. Furthermore, any Ho^{3+} concentration reduction, whether in the core or S_1, would reduce the phonon energy shortage, benefitting phonon-assisted Yb^{3+}–Ho^{3+} ET. It is important to note that while the '<'-distributed S_2@S_3 of [20/10][60/0] was detrimental to inward EM, the far distance from the surface Yb^{3+} ions caused by thick S_2 (~5 nm), and presence for only 20 mol% of Yb^{3+} ions in S_2 for EBT and EM, was somewhat advantageous for reducing outward EM. Additionally, the phonon energy shortage was relatively less severe due to the lower activation of Ho^{3+} ions through inefficient sensitisation. As a result, the efficiency of both Ho^{3+}–Ce^{3+} and Ho^{3+}–Ho^{3+} CR improved, better competing against EBT and reducing outward EM by inhibiting the EBT–EM pathway. Thus, the drawbacks of S_2@S_3 of [20/10][60/0] in our samples were partly mitigated. The relatively similar τ values for S_2@S_3 of [20/10][60/0] and [60/10][60/0] support this analysis (**Table S1** in **SI**).

In comparison, S_2@S_3 of [60/10][20/0] and [60/10][60/0] were relatively more efficient in sensitising energy supply and inward EM. Lengthening *d* by reducing Ho^{3+} concentration in both the core and S_1 had a less negative impact on ET, and EBT was mitigated simultaneously. From another perspective, the phonon energy shortage was much more severe in UCNPs 15 and 16 than in UCNPs 13 and 14, so core@S_1 of [50/10][50/10] with the largest reduction in Ho^{3+} concentration was most beneficial for the efficiency of Ho^{3+}–Ce^{3+} CR and phonon-assisted Yb^{3+}–Ho^{3+} ET, thereby increasing I_{Total}. With 60 mol% of Yb^{3+} ions in S_2, which favoured EBT, the more efficient transitions ($^2F_{7/2} \rightarrow {}^2F_{5/2}$) of Ce^{3+} ions meant that Ho^{3+} ions in the $^5S_2/^5F_4$ state required less time to wait for Ho^{3+}–Ce^{3+} CR, thereby reducing potential energy loss via EBT (see **Note S6** in the **SI**). Similarly, the more efficient Yb^{3+}–Ho^{3+} ET, the less time intermediate $^5I_6$-state and $^5I_7$-state Ho^{3+} ions waited for further sensitisation, leading to more Ho^{3+} ions in the $^5S_2/^5F_4$ and $^5F_5$ states for emission. Because outward EBT–EM was more pronounced in '='-distributed S_2@S_3 of [60/10][60/0], in respond to EBT decrease by Ho^{3+} reducing concentration in both the core and S_1, UCNPs 16 compared to UCNPs 12 showed larger I_{Total} enhancement rate of 47.21%, much higher than the 8.91% increase for UCNPs 15 compared to UCNPs 11. Another relevant example is shown in **Fig. 6b**, where S_2@S_3 of [20/10][20/0] resulted in a higher I_{Total} than [60/10][60/0] for all but the last group. Although UCNPs 16 exhibited worse EBT and surface energy quenching than UCNPs 13, the phonon energy shortage in UCNPs 13–16 was the least severe among the four groups, so phonon-consumed Ho^{3+}–Ce^{3+} CR and Yb^{3+}–Ho^{3+} ET were promoted, leading to a greater increase in I_{Total} for UCNPs 16. Furthermore, the alteration exception for I_G in UCNPs 11 in **Fig. 6b** aligned with our analysis. In UCNPs 11, EBT was worsened by a combination of factors: S_2 of [60/10], the increased waiting time for Ho^{3+}–Ce^{3+} CR due to more severe phonon energy shortage, and shortened *d* by core@S_1 of [50/10][90/10]. More relevant mechanisms would be explained afterwards. As a result, I_G was less enhanced and lower than that of UCNPs 9. More evidence can be found from the τ values. For instance, in the respective group shown in **Fig. 7a–d**, UCNPs 9 and 10 had shorter τ_G and τ_R than UCNPs 5 and 6 due to the overall shorter distance between activated Ho^{3+} ions and the nanoparticle surface; UCNPs 13 and 15 had the longest τ_G and τ_R due to moderate *d* values and the

least phonon energy shortage.

In conclusion, I_{Total} changed with the Ho^{3+} concentration distributions in the core and S_1 due to variations in *d* and phonon energy shortages. A reduction in Ho^{3+} concentration solely in the core correlated with a relatively inefficient S_2@S_3, whereas a reduction in both the core and S_1 correlated with an efficient S_2@S_3.

Interestingly, as shown in **Table S1**, UCNPs 9 and 11 exhibited higher τ_G and τ_R than UCNPs 1 and 3, respectively, which seemed contradictory to our hypothesis that the *d* sequence of core@S_1 should be [50/10][90/10] < [90/10][90/10]. However, as discussed earlier for I_{Total} variations in **Fig. 7a–d**, alleviating phonon energy shortage by reducing Ho^{3+} concentration can increase the efficiency of Ho^{3+}–Ce^{3+} CR and phonon-assisted Yb^{3+}–Ho^{3+} ET, populating more Ho^{3+} ions in $^5S_2/^5F_4$ and $^5F_5$ states. Furthermore, the shortened overall Yb^{3+}–Ho^{3+} distance due to core@S_1 of [50/10][90/10] promoted Yb^{3+}–Ho^{3+} ET, thereby activating more Ho^{3+} ions. Consequently, the probability of nonradiative decay possibility partly decreased with larger Ho^{3+} population on emitting states. And when EBT and surface energy quenching were not that severe from S_2@S_3 of [20/10][20/0] and [60/10][20/0] in UCNPs 9 and 11, their τ_G and τ_R might be higher than those of UCNPs 1 and 3. In contrast, UCNPs 10 and 12 exhibited lower τ_G and τ_R than UCNPs 2 and 4 due to the more severe EBT and surface energy quenching from S_2@S_3 of [20/10][60/0] and [60/10][60/0]. This result indicated that, under reduced EBT and surface energy quenching by double active shells, Ho^{3+} concentration distributions could also decide τ values by influencing phonon energy shortage. The energy mechanisms in Ce^{3+}-doped Ho@Yb UCNPs are highly complex and require careful analysis.

The distribution of Ho^{3+} concentrations in Ho@Yb UCNPs had a greater impact on the τ values. In conventional low-doped core–multi-shell structures, activators distributed throughout the UCNPs typically exhibited a consistent emission tendency. Emitters associated with each characteristic peak were subjected to similar sensitisation and energy loss conditions. However, in Ho@Yb structures, as discussed above in relation to **Fig. 2**, within *d*, Ho^{3+} activators located near surface Yb^{3+} ions predominantly emitted green UCL, whereas those situated deeper primarily emitted red UCL. This indicates that I_G-favoured Ho^{3+} ions inherently experienced greater EBT and surface energy quenching compared to I_R-favoured ones. Because τ is highly sensitive to EBT and surface energy quenching, τ_G should accordingly be smaller. Following the reduction of Ho^{3+} concentration in the S_1 layer of our CSSS samples, *d* increased, leading to a greater proportion of newly added, deeper Ho^{3+} ions that were I_R-favoured and exhibited longer τ values—thereby contributing to an overall rise in τ_R. In contrast, first, the I_G-favoured Ho^{3+} ions saw less benefit from the reduced Ho^{3+}–Ho^{3+} CR than those in Ce^{3+}-doped CSS UCNPs. This is because Ce^{3+} ions were doped simultaneously in the core, S_1 and S_2 layers, allowing the phonon energy release from the reduced Ho^{3+} concentration to be readily utilised by Ce^{3+} dopants, increasing the overall Ho^{3+}–Ce^{3+} CR efficiency. Moreover, given the S_3 layer's thickness of ~3.5 nm, some Ce^{3+} ions doped in S_2 could interact with surface groups instead for $^2F_{7/2} \rightarrow {}^2F_{5/2}$ transitions, further enhancing Ho^{3+}–Ce^{3+} CR. Consequently, I_G-favoured Ho^{3+} ions were subjected to more non-radiative Ho^{3+}–Ce^{3+} CR. Second, at higher Ho^{3+} concentrations, more excited-state Ho^{3+} ions were located in close proximity. While this led to competition for Yb^{3+}–Ho^{3+} ET, it also allowed the ions to mutually shield each other from surface energy quenching (**Fig. 7e–f**). Conversely, when the Ho^{3+} concentration in S_1 was reduced, fewer activated green emitters surrounded one another, increasing the likelihood of individual decay from the $^5S_2/^5F_4$ state via Ho^{3+}–Ce^{3+} CR, SQs, and especially EBT, due to the phonon energy shortage.

Although the reduced ET competition could activate more Ho^{3+} ions, many of these were inside and I_R-favoured. Only those relatively close to the surface and distant from S_2-doped Ce^{3+} ions were I_G-favoured. The influences from EBT and surface energy quenching on τ_G turned less reduced. Therefore, the overall increase in τ_G was smaller than that of τ_R, or τ_G might even decrease. It is worth noting that fewer Ho^{3+} ions in front in S_1 could indeed increase EBT in the I_R-favoured region, but this effect was negligible in light of the contribution of the newly added deep Ho^{3+} ions that were I_R-favoured, and the remaining 50 mol% of Ho^{3+} ions near the S_2/S_2 interface. The τ values reported in **Table 1** support our analysis. For structures with $S_2@S_3$ configurations of [60/10][60/0] and [20/10][60/0], which facilitated greater access to EBT and SQs, τ_G exhibited lower increase rates of 11.49% and 11.47%, compared with 31.41% and 29.16% for τ_R, respectively, after reducing Ho^{3+} concentration solely in S_1. This disparity narrowed to 62.59% and 63.28% versus 63.95% and 71.26%, respectively, when the $S_2@S_3$ configuration was altered to [60/10][20/0] and [20/10][20/0] for less EBT and surface energy quenching. Additionally, τ_R increased more significantly than τ_G when transitioning from core@S_1 configurations of [90/10][90/10] or [50/10][90/10] to [50/10][50/10] (**Table S2** in **SI**), further indicating the effective Ho^{3+}–Ce^{3+} CR mediated by Ce^{3+} ions in S_2 and the reduced shielding from fewer neighbouring Ho^{3+} ions. In summary, in Ho@Yb UCNPs, reducing Ho^{3+} concentration in S_1 led to a greater enhancement in τ_R than in τ_G. This outcome can be attributed to the spatial distinction between I_G-favoured and I_R-favoured Ho^{3+} ions, the shielding effect of neighbouring Ho^{3+} ions and the pervasive Ho^{3+}–Ce^{3+} CR enabled by Ce^{3+} dopants present across the core, S_1 and S_2 layers.

In particular, UCNPs 5–8 generally exhibited the lowest I_{Total} within their respective groups in **Fig. 7a–d**. This phenomenon provides further insight into how variations in Yb^{3+} and Ho^{3+} concentration distributions affect *d*. Both the core@S_1 structure [90/10][50/10] and the $S_2@S_3$ structure [60/10][20/0] resulted in a lengthened *d*, albeit via entirely different mechanisms. In the former, the lengthening was caused by a reduction in Ho^{3+} concentration within S_1, which forced Yb^{3+} ions to locate ground-state Ho^{3+} ions situated deeper within the structure as energy acceptors (**Fig. 3e**). With the presence of Ce^{3+} ions in S_2 and no reduction in Ho^{3+} concentration in the core, the inward supply of sensitising energy was not significantly enhanced due to the persistent shortage of phonon energy. Coupled with the increased Yb^{3+}–Ho^{3+} ET distance, the number of newly activated Ho^{3+} ions in the core likely did not compensate for the loss caused by the Ho^{3+} concentration cut in S_1. Given that S_1 is ~4 nm thick—sufficient to cause a notable change in ET distance under Ho^{3+} reduction—the most probable outcome was a decreased population of Ho^{3+} ions in the $^5S_2/^5F_4$ and $^5F_5$ excited states. Although τ of these excited Ho^{3+} ions may have been prolonged, as previously discussed, I_{Total} is determined by both the number and τ of emitting states. Thus, in our CSSS UCNPs, the overall effect was a reduction in I_{Total}. This underscores that increasing the overall Yb^{3+}–Ho^{3+} distance to suppress EBT—at the cost of diminished Yb^{3+}–Ho^{3+} ET efficiency—is not an optimal strategy. By contrast, in the $S_2@S_3$ structure with a '>'-gradient, *d* was lengthened primarily through increased inward sensitising energy and reduced EBT–EM outward. As a result, more Ho^{3+} ions were effectively activated (**Fig. 7g**), and they experienced less EBT and surface energy quenching. This yielded a greater number of Ho^{3+} ions in emissive states with extended τ, ultimately enhancing I_{Total}. This is supported by **Fig. 7a–d**, where the I_{Total} reduction between UCNPs 3 and 7 was just 6.50%, notably less than the respective decreases of 12.03%, 39.98% and 38.74% observed between UCNP pairs 1 and 5, 2 and 6 and 4 and 8. This suggests that the improved Yb^{3+}–Ho^{3+} ET and enhanced surface energy protection afforded by the $S_2@S_3$ of

[60/10][20/0] partially compensated for the extended ET distance imposed by core@S_1 of [90/10][50/10]. Nonetheless, EBT remained relatively significant in S_2 of [60/10], and the protective effect of surrounding Ho^{3+} ions was weakened by core@S_1 of [90/10][50/10]. To exacerbate matters, as discussed previously, the probability of EBT increases under conditions of continued phonon energy shortage. Therefore, I_{Total} ultimately declined. Among the other UCNP pairs, UCNPs 1 and 5 and 2 and 6 suffered from inefficient ET, while UCNP pairs 2 and 6 and 4 and 12 exhibited worsened surface energy protection. These factors proved more detrimental to core@S_1 of [90/10][50/10] than UCNP pair 3 and 7, explaining the greater I_{Total} reductions observed. Notably, as shown in **Fig. 3b**, CSS UCNPs with the configuration [90/10][50/10][60/0] had a higher I_{Total} than those with [90/10][90/10][60/0], implying a role for the number of structural layers. EBT and surface energy quenching effects were more pronounced in Ce^{3+}-doped CSS structures compared to CSSS ones, which might allow the beneficial impact of reduced EBT to outweigh the negative consequence of lower ET efficiency when *d* is increased via Ho^{3+} concentration reduction in S_1.

Moreover, whether using S_2 of [60/10] or [20/10], core@S_1 of [50/10][90/10] consistently achieved higher I_{Total} than [90/10][50/10], further underscoring the precedence of ET efficiency over EBT with respect to the overall Yb^{3+}–Ho^{3+} distance. This observation also highlights a distinct feature of Ce^{3+}-doped Ho@Yb structures: due to the separation of sensitiser and activator by shells, Ho@Yb UCNPs depend far more on the spatial proximity between sensitiser and activator ions than traditional co-doped UCNPs do for efficient UCL. Additionally, with the presence of '>' Yb^{3+} concentration profiles and Ce^{3+} doping across the core, S_1 and S_2 layers, phonon energy shortage became particularly significant. The shortage is primarily caused by phonon-consuming Yb^{3+}–Ho^{3+} ET and Ho^{3+}–Ce^{3+} CR processes. Therefore, reducing Ho^{3+} concentration is necessary to eliminate a portion of substitutable NR and suppress Ho^{3+}–Ho^{3+} CR. However, this adjustment must be made with caution, as the potentially associated increase in *d* should be avoided to optimise nanoparticle performance. Another justified inference concerns the core@S_1 structure of [50/10][90/10]: the additional sensitising energy in S_1—compared to [90/10][90/10]—would primarily be transferred to Ho^{3+} ions near the S_1/S_2 interface, rather than to ions located deeper or beyond *d*. This is because the inward flow of sensitising energy was not substantially improved, and the ET efficiency remained highly dependent on the Yb^{3+}–Ho^{3+} distance (**Fig. 7h**). As such, *d* was shortened. In contrast, for core@S_1 of [90/10][50/10], surplus sensitising energy in the core was likely transferred to Ho^{3+} ions near the core/S_1 interface—regions that are deeper or already beyond *d* (**Fig. 7i**), resulting in a partial increase in *d*. This further supports our earlier conclusion that the order of *d* values for core@S_1 structures follows the sequence: [50/10][90/10] < [90/10][90/10] < [50/10][50/10] < [90/10][50/10], under the same Yb^{3+} sensitising conditions. In summary, changes in *d* induced by varying Yb^{3+} and Ho^{3+} concentration distributions follow distinct mechanisms. Reducing Ho^{3+} concentration solely in the S_1 layer is not conducive to I_{Total} enhancement in our CSSS UCNPs.

Yb^{3+} lifetimes of can provide more proof for our analysis (see **Note S7** in **SI**). Besides, further detailed variations in I_G, I_R, G/R ratios and τ values for UCNPs 1–16, presented in **Fig. 7a–d**, **S15** and **Table S1**, are consistent with this discussion (see **Note S8** in **SI**). The line charts of UCL properties for Ce^{3+}-doped UCNPs (**Fig. 7a–d**) clearly demonstrate the significant influence of both Yb^{3+} and Ho^{3+} concentration distributions within CSSS structures. Overall, compared to CSS UCNPs, the UCL intensity was enhanced in CSSS structures. Additionally, with Ce^{3+} doping in the core, S_1 and S_2 layers, the G/R ratios were lower and more stably controlled around 1. Notably,

UCNPs 11 and 15 exhibited the most optimal UCL properties in terms of G/R ratio and I_{Total}, respectively. These two samples also possessed comparable quantum yields as conventional low-doped UCNPs (**Fig. S16**).

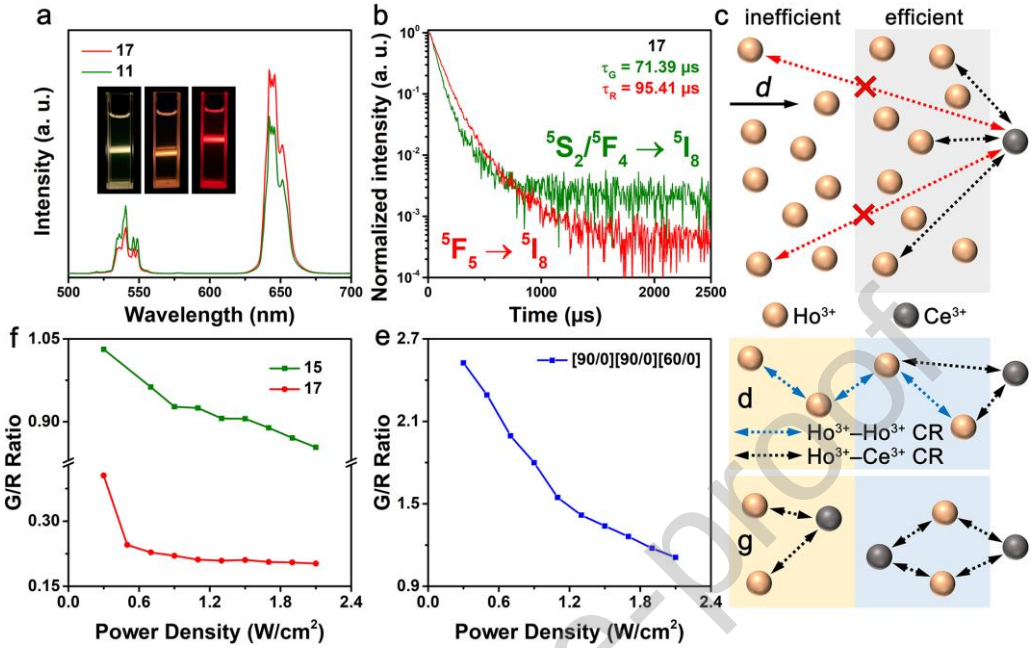

Figure 8. (a) UCL spectra of UCNPs 11 ([50/10][90/10][60/10][20/0], $NaHoF_4$:10%Ce^{3+},40%Gd^{3+}@$NaHoF_4$:10%Ce^{3+}@$NaGdF_4$:60%Yb^{3+},10%Ce^{3+}@$NaGdF_4$:20%Yb^{3+}) and 17 ([50/0][90/0][60/10][20/0], $NaHoF_4$:50%Gd^{3+}@$NaHoF_4$:10%Gd^{3+}@$NaGdF_4$:60%Yb^{3+},10%Ce^{3+}@$NaGdF_4$:20%Yb^{3+}). Inserted images from left to right: UCL photos of UCNPs 15 ([50/10][50/10][60/10][20/0], $NaHoF_4$:10%Ce^{3+},40%Gd^{3+}@$NaHoF_4$:10%Ce^{3+},40%Gd^{3+}@$NaGdF_4$:60%Yb^{3+},10%Ce^{3+}@$NaGdF_4$:20%Yb^{3+}), 11, and 17 for better comparison. (b) Decay curves of green UCL at 540 nm and red UCL at 645 nm of UCNPs 17. (c) Schematic graphs of *d* decrease due to Ce^{3+} doping only in S_2. (d) Schematic graphs of most possible CR mechanisms in UCNPs 17. (e)–(f) Line charts of G/R ratio variations with power density of UCNPs [90/0][90/0][60/0], 15 and 17. (g) Schematic graphs of most possible CR mechanisms in UCNPs 11.

The UCL spectrum and decay curves of [50/0][90/0][60/10][20/0] UCNPs (numbered as 17) are shown in **Fig. 8a–b**, respectively. Interestingly, compared with UCNPs 11, UCNPs 17 exhibited approximately the same I_{Total} but a lower G/R ratio of 0.23, compared to 0.43 for UCNPs 11, as well as shorter τ_G and τ_R values of 71.39 and 95.41 μs, respectively. Based on our previous study, Ce^{3+} doping in S_2 was more effective than in the core and S_1 due to reduced phonon energy shortage through energy interactions with nanoparticle surface groups such as CH_2.[17] Because the quantity of Ce^{3+} ions was greater and doped in the core, S_1 and S_2, the phonon energy shortage in UCNPs 11 would be more severe than in UCNPs 17. The $^5S_2/^5F_4$-state Ho^{3+} ions required longer intervals for Ho^{3+}–Ce^{3+} CR, which was not conducive to a lower G/R ratio and EBT possibility. However, the UCNPs 17 had similar sizes to the UCNPs 1–16 (**Fig. S17**), meaning the core@S_1 structure for UCNPs 17 was relatively large, making it difficult for S_2-doped Ce^{3+} ions to initiate relatively efficient CR with deep Ho^{3+} ions. The majority of I_R-favoured Ho^{3+} emitters were likely located nearer to the S_1/S_2 interface and underwent more EBT than those in UCNPs 11. The final result was a reduction in τ_R for UCNPs 17. The low G/R ratio of UCNPs 11, with a shortened overall distance between Ho^{3+} and S_2-doped Ce^{3+} ions (**Fig. 7a–d**) partly supports this proposed mechanism.

Accordingly, *d* of UCNPs 17 should be shorter than that of UCNPs 11, but the red-emitting Ho^{3+} ions within *d* became more efficient to increase I_R (**Fig. 8c**). It is worth pointing out that in our previous research,[17] the $NaHoF_4$ core was only ~6 nm, enabling easy coverage of core-doped Ho^{3+} ions by CR from shell-doped Ce^{3+} ions, which had relatively negligible effect on the locations of I_R-favoured Ho^{3+} emitters. Therefore, τ_R was longer with Ce^{3+} doping in the shell than in the core. This phenomenon indicated that the UCL analysis was complex for Ho@Yb UCNPs, where even core–shell sizes could alter UCL mechanisms and properties. Regarding τ_G, its decrease confirmed the efficiency of S_2-doped Ce^{3+} in depopulating $^5S_2/^5F_4$-state Ho^{3+} ions in UCNPs 17.

CR mechanisms were then compared for UCNPs 11 and 17. The most likely situation for UCNPs 17 involved Ho^{3+}–Ho^{3+} CR dominance in the core and both Ho^{3+}–Ho^{3+} and Ho^{3+}–Ce^{3+} CR dominance in S_1 (**Fig. 8d**), with the location differences between I_G-favoured and I_R-favoured Ho^{3+} ions in Ho@Yb structures still present. As shown in **Figs. 8e–f** and **S18**, similar to our previous results,[31] with a power density change from 0.3 to 2.1 W/cm^2, the G/R ratio values gradually decreased from 0.41 to 0.20, 1.03 to 0.85 and 2.52 to 1.11 for Ce^{3+}-doped CSSS 17 and 15 and Ce^{3+}-free CSS [90/0][90/0][60/0] UCNPs, respectively. When the inward sensitising energy supply increased with higher power density, deep Ho^{3+} ions had a better chance of being activated for emission. As they were farther from Ce^{3+} ions in UCNPs 17, the decreased G/R ratio proved that they could participate in alternative Ho^{3+}–Ho^{3+} CR for relatively efficient red emission. In UCNPs 15, with less Ho^{3+}–Ho^{3+} CR from fewer Ho^{3+} ions competing for phonon energy, Ho^{3+}–Ce^{3+} CR of Ce^{3+} dopants in the core and S_1 should be more efficient than in UCNPs 11. Despite this, the G/R ratio decreased with increasing power density, confirming the validity of our initial assumption that for our samples in this research, the Ho@Yb feature regarding location differences between I_G-favoured and I_R-favoured Ho^{3+} ions remained with Ce^{3+} dopants in the core and S_1. From another perspective, compared with traditional $NaGdF_4$:Yb^{3+},Ce^{3+},Ho^{3+} UCNPs, where the G/R ratio remained nearly constant with increasing pump power, Ce^{3+}-doped Ho@Yb UCNPs exhibited a colour change response to pump power, offering greater application potential, such as for sensing and anti-counterfeiting. Additionally, the larger reduction in the G/R ratio in [90/0][90/0][60/0] UCNPs was caused by insufficient energy supply and protection by the single S_2 of [60/0], which activated fewer I_R-favoured Ho^{3+} ions at 0.3 W/cm^2. For UCNPs 11, Ce^{3+} dopants in the core@S_1 could compete with those in S_2 for phonon energy, and the most likely situation would be Ho^{3+}–Ce^{3+} CR dominance in both the core and S_1 (**Fig. 8g**). However, part of Ho^{3+}–Ho^{3+} CR could cooperate with Ho^{3+}–Ce^{3+} CR1 to enhance I_R through cycles of $^5I_6$ (Ho_1^{3+}) + $^2F_{5/2}$ (Ce^{3+}) → $^5I_7$ (Ho_1^{3+}) + $^2F_{7/2}$ (Ce^{3+}), followed by $^5I_7$ (Ho_1^{3+}) + $^5F_4/^5S_2$ (Ho_2^{3+}) → $^5I_6$ (Ho_1^{3+}) + $^5F_5$ (Ho_2^{3+}), which would depopulate $^5F_4/^5S_2$-state Ho^{3+} ions, as in Ho^{3+}–Ce^{3+} CR2 (**Fig. 2**). In this sense, the relative inefficiency of CR2 compared with CR1 was offset to some degree. To summarise, UCNPs 11 and 17 had different UCL properties and mechanisms, with better performance in τ and G/R ratio, respectively. Ce^{3+}-doped Ho@Yb UCNPs displayed tunable UCL colour with pump power, offering wider application possibilities.

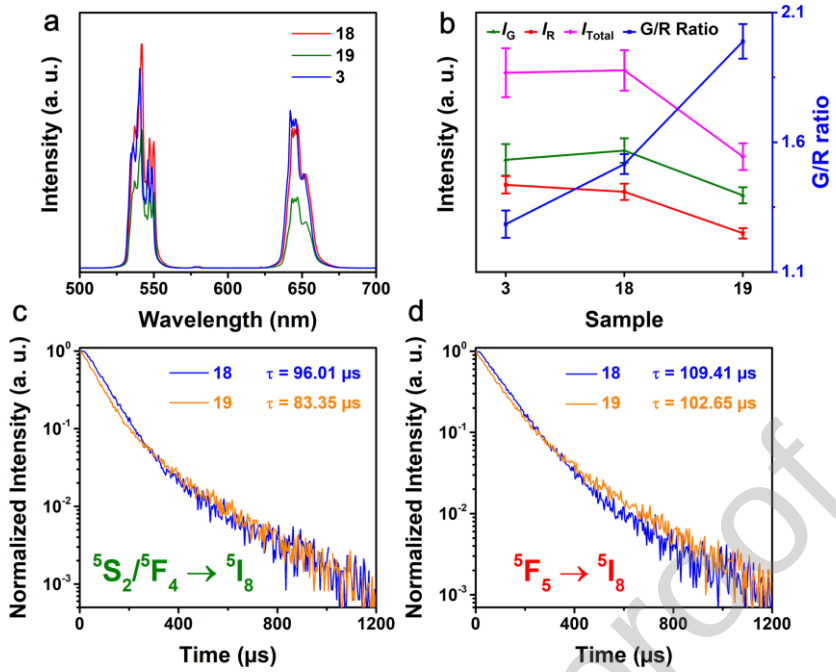

Figure 9. (a) UCL spectra, (b) line charts of UCL properties and (c)–(d) decay curves of green UCL at 540 nm and red UCL at 645 nm of UCNPs 18 ([90/10][90/0][60/0][20/0], $NaHoF_4$:10%Ce^{3+}@$NaHoF_4$:10%Gd^{3+}@$NaGdF_4$:60%Yb^{3+}@$NaGdF_4$:20%Yb^{3+}) and 19 ([90/0][90/10][60/0][20/0], $NaHoF_4$:10%Gd^{3+}@$NaHoF_4$:10%Ce^{3+}@$NaGdF_4$:60%Yb^{3+}@$NaGdF_4$:20%Yb^{3+}). UCL spectrum and properties of UCNPs 3 ([90/10][90/10][60/10][20/0], $NaHoF_4$:10%Ce^{3+}@$NaHoF_4$:10%Ce^{3+}@$NaGdF_4$:60%Yb^{3+},10%Ce^{3+}@$NaGdF_4$:20%Yb^{3+}) are added for better comparison.

Finally, the influences of Ce^{3+} doping only in core or S_1 were studied. **Fig. S19** and **9a–b** show the TEM images, UCL spectra and properties of [90/10][90/0][60/0][20/0] and [90/0][90/10][60/0][20/0] UCNPs (numbered as 18 and 19, respectively). UCNPs 3 were included for better comparison. Clearly, UCNPs 18 and 19 exhibited similar sizes to the UCNPs 1–16, and the sequence of G/R ratio values was 1.28 of UCNPs 3 < 1.52 of UCNPs 18 < 1.99 of UCNPs 19, indicating that Ce^{3+} dopants available in multiple layers were advantageous for a lower G/R ratio, and that S_1-doped Ce^{3+} ions were relatively less effective. Because S_1 was ~8 nm away from the nanoparticle surface, S_1-doped Ce^{3+} ions were most likely to consume lattice phonons for Ho^{3+}–Ce^{3+} CR, just as core-doped Ce^{3+} ions did. However, S_1-located Ho^{3+} ions were closer to the sensitisers and required more phonon energy for Yb^{3+}–Ho^{3+} ET than core-located Ho^{3+} ions. Therefore, in UCNPs 19, the phonon -consuming Ho^{3+}–Ce^{3+} CR and Yb^{3+}–Ho^{3+} ET together within S_1 went against efficient phonon energy usage and conflicted with each other more than when separated by the core and S_1 in UCNPs 18. Note that, given the lowest G/R ratio of UCNPs 17, the average Ho^{3+}–Ce^{3+} distance for CR should not be as important as the Yb^{3+}–Ho^{3+} distance for ET in our CSSS samples. For UCNPs 3, with Ce^{3+} doping in multiple layers, Ho^{3+}–Ce^{3+} CR suppressed inferior Ho^{3+}–Ho^{3+} CR across core@S_1, allowing for better overall phonon energy allocation than in UCNPs 19, as evidenced by the slightly lower I_{Total} than for UCNPs 18 in **Fig. 9b**. In contrast, the I_{total} of UCNPs 19 dropped markedly. Further evidence was provided by the decay curves (**Fig. 9c–d**). Fitted τ_G and τ_R values were 83 and 101.95, 96.01 and 109.41 and 83.35 and 102.65 μs for UCNPs 3, 18 and 19, respectively. Reduced competition for phonon energy between Ho^{3+}–Ce^{3+} CR and Yb^{3+}–Ho^{3+} ET not only shortened the needed CR-waiting time for $^5S_2/^5F_4$-state Ho^{3+} ions to

lessen EBT and surface energy quenching but also populated more $^5S_2/^5F_4$-state and $^5F_5$-state Ho^{3+} ions as emitters or shielded other surrounding emitters, leading to the longest τ_G and τ_R for UCNPs 18. Interestingly, UCNPs 3 obtained τ_G and τ_R values very close to those of UCNPs 19, even though there were additional Ce^{3+} dopants in the core and S_2. This result confirmed the superiority of Ce^{3+} doping in multiple layers and suggested that not all Ce^{3+} dopants took effect, but only those optimising phonon energy usage did to keep the overall Ho^{3+}–Ce^{3+} CR as efficient as possible, such as those near the nanoparticle surface or in positions conducive to phonon acquisition or Ho^{3+}–Ho^{3+} CR. Another typical example was UCNPs 11, where, under enhanced Yb^{3+}–Ho^{3+} ET by both '>'-distributed Yb^{3+} concentrations and shortened Yb^{3+}–Ho^{3+} distances, the severe phonon energy shortage meant that most of the active Ce^{3+} ions were rationally S_2-doped. Therefore, apart from the previously mentioned EBT, the low I_G and G/R ratio was also determined by the distance to the S_2-doped Ce^{3+} ions. In contrast, the significant increase in the G/R ratio from CSS [90/10][50/10][60/0] to [50/10][50/10][60/0] UCNPs (**Fig. 3b**) clearly demonstrated the inferiority of Ce^{3+} doping only in the core and S_1, as did not optimise phonon energy allocation throughout the UCNPs for efficient Ho^{3+}–Ce^{3+} CR. In a nutshell, for the [90/0][90/0][60/0][20/0] structure, Ce^{3+} doping solely in the core was slightly more conducive to I_{total} and τ, but Ce^{3+} doping in multiple layers achieved a lower G/R ratio.

Conclusion

In conclusion, a series of Ce^{3+}-doped and Ce^{3+}-free core–multi-shell UCNPs, highly doped with Ho^{3+} and Yb^{3+} ions, were successfully synthesised using the oleate method. The concentration distributions of Ho^{3+} in the core and first shell (S_1), and Yb^{3+} in the second and third layers (S_2 and S_3), significantly influenced Ce^{3+}-finetuned upconversion luminescence (UCL) but by different energy mechanisms. Except in double-shell UCNPs with an S_2 layer of $NaGdF_4$:20%Yb^{3+}, all Ho^{3+} ions participated in UCL. Ho^{3+} ions in the core primarily engaged in Ho^{3+}–Ho^{3+} CR, while those in S_1 contributed mainly to emission and Ho^{3+}–Ho^{3+} CR. In the Ce^{3+}-doped triple-shell UCNPs, reducing the Ho^{3+} concentration in the core or S_1 can alter *d* (within which emission were relatively effective) by modulating the proximity of Ho^{3+} energy acceptors to Yb^{3+} donors, which in turn influenced the Yb^{3+}–Ho^{3+} ET, EBT and surface energy quenching. In contrast, higher Yb^{3+} concentrations in S_2 and lower concentrations in S_3 resulted in an increased inward sensitising energy supply and reduced EBT and surface energy quenching, thus extending *d*. The reduction of Ho^{3+} concentrations, especially in the S_1 layer, mitigated phonon energy shortage by decreasing Ho^{3+}–Ho^{3+} CR to enhance phonon-consumed Ho^{3+}–Ce^{3+} CR and Yb^{3+}–Ho^{3+} ET, and to partly decrease surface quenching. However, this also decreased the energy shielding effect provided by surrounding activated Ho^{3+}. Furthermore, the distribution of Yb^{3+} ions favourable for ET was found to partially worsen phonon energy shortage. The number of layers in the UCNPs affected how these Ho^{3+} and Yb^{3+} concentrations influenced UCL. The $NaHoF_4$:10%Ce^{3+},40%Gd^{3+}@$NaHoF_4$:10%Ce^{3+}@$NaGdF_4$:10%Ce^{3+},60%Yb^{3+}@$NaGdF_4$:20%Yb^{3+} UCNPs exhibited generally optimal UCL performance, with a G/R ratio of 0.43, a red UCL decay time of 164.97 μs and a quantum yield of 1.23%. When Ce^{3+} doping was confined to a single layer, UCL properties were less favourable compared to multi-layers. Doping Ce^{3+} only in the S_2 shell reduced the G/R ratio but also shortened decay times, leading to altered CR mechanisms. Notably, the Ce^{3+}-doped core–multi-shell UCNPs displayed tunable G/R ratios with pump power, an advantage over traditional $NaGdF_4$:Yb^{3+},Ce^{3+},Ho^{3+} UCNPs. These findings provide a

comprehensive understanding of Ce^{3+} doping in core–multi-shell and highly doped UCNPs, offering strategies for fine-tuning UCL properties and expanding the multifunctional applications of $NaHoF_4$-based materials.

ASSOCIATED CONTENT

Supporting Information.

This material is available free of charge via the Internet at https://www.sciencedirect.com/journal/journal-of-colloid-and-interface-science.

Experiment and characterization methods, Notes S1–8, Tables S1–2, and Figures S1–19 were provided.

Figure contents: TEM images, size distribution diagrams and XRD patterns of selected core, core-shell, core–double-shell and core–triple-shell UCNPs; High-resolution TEM images of [50/10][90/10][20/10][60/0] and [90/10][90/10][60/10][20/0] UCNPs; Elemental mapping images of [90/10][90/10][60/10][20/0] UCNPs; UCL spectra of [50/10][50/10][20/0] and [50/10][50/10][60/0] UCNPs; UCL spectra under varied power densities of [90/0][90/0][60/0], [50/10][50/10][60/10][20/0] and [50/0][90/0][60/10][20/0] UCNPs; G/R ratios of UCNPs 1–16; Decay curves of 540 nm green and 645 nm red UCL of [100/0][90/10][60/0], [90/10][90/10][60/0], [90/10][50/10][60/0] and [50/10][50/10][60/0] UCNPs; Quantum yields of $NaGdF_4$:18%Yb^{3+},2%Ho^{3+}, [50/10][90/10][60/10][20/0] and [50/10][50/10][60/10][20/0] UCNPs; Pump power dependence of [90/10][50/10][60/0] UCNPs.

AUTHOR INFORMATION

Corresponding Author

* shenlonghai@sylu.edu.cn (Longhai Shen)

* wangyiwei@symc.edu.cn (Yiwei Wang)

Notes

The authors declare no competing financial interest.

ACKNOWLEDGMENT

The work was financially supported by the National Natural Science Foundation of China (12274304), the fund of Department of Education of Liaoning Province (JYTQN2023046), Team Construction Project of Liaoning Province Education Department (LJ222410164013), Liaoning Provincial Natural Science Foundation (2024010751-JH3/107).

References

(1) Wang, G.; Peng, Q.; Li, Y. Upconversion Luminescence of Monodisperse CaF_2:Yb^{3+}/Er^{3+} Nanocrystals. *J. Am. Chem. Soc.* **2009**, *131* (40), 14200-14201. DOI: 10.1021/ja906732y.

(2) Li, Y.; Xu, J.; Hu, T.; Shi, G.; Peng, Y.; Qiao, F.; Zhang, L.; Zhao, C.; Kuang, Y.; Shen, L. Synthesis and Upconversion Luminescence Fine-tuning of Yb^{3+}/Ho^{3+}-Doped Indium and Gallium Oxide Nanoparticles. *Inorg. Chem.* **2024**, *63* (37), 17032-17042. DOI: 10.1021/acs.inorgchem.4c02701.

(3) Schroter, A.; Märkl, S.; Weitzel, N.; Hirsch, T. Upconversion Nanocrystals with High Lanthanide Content: Luminescence Loss by Energy Migration versus Luminescence Enhancement by Increased NIR Absorption. *Adv.*

Funct. Mater. **2022**, *32* (26), 2113065. DOI: 10.1002/adfm.202113065.

(4) Liu, Y.; Lu, Y.; Yang, X.; Zheng, X.; Wen, S.; Wang, F.; Vidal, X.; Zhao, J.; Liu, D.; Zhou, Z.; et al. Amplified stimulated emission in upconversion nanoparticles for super-resolution nanoscopy. *Nature* **2017**, *543* (7644), 229-233. DOI: 10.1038/nature21366.

(5) Chen, C.; Liu, B.; Liu, Y.; Liao, J.; Shan, X.; Wang, F.; Jin, D. Heterochromatic Nonlinear Optical Responses in Upconversion Nanoparticles for Super-Resolution Nanoscopy. *Adv. Mater.* **2021**, *33* (23), 2008847. DOI: 10.1002/adma.202008847.

(6) Liu, B.-T.; Huang, T.-H.; Wang, T.-L.; Hsu, C.-C. Enhanced efficiency of low-temperature fabricated dye-sensitized solar cells by incorporating upconversion nanoparticles. *Sol. Energy* **2021**, *227*, 1-7. DOI: 10.1016/j.solener.2021.08.076.

(7) Khare, A. A critical review on the efficiency improvement of upconversion assisted solar cells. *J. Alloys Compd.* **2020**, *821*, 153214. DOI: 10.1016/j.jallcom.2019.153214.

(8) Huang, J.; Yan, L.; An, Z.; Wei, H.; Wang, C.; Zhang, Q.; Zhou, B. Cross Relaxation Enables Spatiotemporal Color-Switchable Upconversion in a Single Sandwich Nanoparticle for Information Security. *Adv. Mater.* **2023**, *36* (13), 2310524. DOI: 10.1002/adma.202310524.

(9) Przybylska, D.; Grzyb, T.; Erdman, A.; Olejnik, K.; Szczeszak, A. Anti-counterfeiting system based on luminescent varnish enriched by NIR- excited nanoparticles for paper security. *Sci. Rep.* **2022**, *12* (1), 19388. DOI: 10.1038/s41598-022-23686-9.

(10) Suo, H.; Zhu, Q.; Zhang, X.; Chen, B.; Chen, J.; Wang, F. High-security anti-counterfeiting through upconversion luminescence. *Mater. Today Phys.* **2021**, *21*, 100520. DOI: 10.1016/j.mtphys.2021.100520.

(11) Chen, H.; Ding, B.; Ma, P. a.; Lin, J. Recent progress in upconversion nanomaterials for emerging optical biological applications. *Adv. Drug Delivery Rev.* **2022**, *188*, 114414. DOI: 10.1016/j.addr.2022.114414.

(12) Li, H.; Liu, H.; Wong, K.-L.; All, A. H. Lanthanide-doped upconversion nanoparticles as nanoprobes for bioimaging. *Biomater. Sci.* **2024**, *12* (18), 4650-4663. DOI: 10.1039/D4BM00774C.

(13) Kang, C.; Zuo, X.; Zhao, L.; Ren, C.; Wang, Y.; Liu, Y.; He, X.; Li, X.; Han, G. Red emission upconversion of $NaYF_4$: Yb^{3+}/Er^{3+} nanoparticles: Rapid preparation via single-mode focused microwave method and their application in cell imaging. *Opt. Mater.* **2023**, *143*, 114165. DOI: 10.1016/j.optmat.2023.114165.

(14) Liu, H.; Yan, L.; Huang, J.; An, Z.; Sheng, W.; Zhou, B. Ultrasensitive Thermochromic Upconversion in Core–Shell–Shell Nanoparticles for Nanothermometry and Anticounterfeiting. *J. Phys. Chem. Lett.* **2022**, *13* (10), 2306-2312. DOI: 10.1021/acs.jpclett.2c00005.

(15) Huang, G.; Wu, X.; Zhan, S.; Liu, Y. Simultaneous enhancement of fluorescence intensity, thermometric sensitivity and SNR of upconversion thermometers via optical field localization. *J. Mater. Chem. C* **2022**, *10* (13), 5190-5199. DOI: 10.1039/D1TC05838J.

(16) Wu, J.; Wu, J.; Wei, W.; Zhang, Y.; Chen, Q. Upconversion Nanoparticles Based Sensing: From Design to Point-of-Care Testing. *Small* **2024**, *20* (29), 2311729. DOI: 10.1002/smll.202311729.

(17) Xu, J.; Wang, B.; Shi, G.; Hu, T.; Yang, P.; Kuang, Y.; Shen, L. Exploring energy mechanisms involved in the luminescence reduction due to Ce^{3+} doping via core-multishell upconversion nanoparticles highly doped with Ho^{3+} and Yb^{3+}. *Ceram. Int.* **2024**, *50* (10), 17593-17603. DOI: 10.1016/j.ceramint.2024.02.248.

(18) Liu, X.; Yan, C. H.; Capobianco, J. A. Photon upconversion nanomaterials. *Chem. Soc. Rev.* **2015**, *44* (6), 1299-1301. DOI: 10.1039/c5cs90009c.

(19) Heer, S.; Kömpe, K.; Güdel, H. U.; Haase, M. Highly Efficient Multicolour Upconversion Emission in Transparent Colloids of Lanthanide-Doped NaYF4 Nanocrystals. *Adv. Mater.* **2004**, *16* (23-24), 2102-2105. DOI: 10.1002/adma.200400772.

(20) Guo, X.; Pu, R.; Zhu, Z.; Qiao, S.; Liang, Y.; Huang, B.; Liu, H.; Labrador-Páez, L.; Kostiv, U.; Zhao, P.; et al.

Achieving low-power single-wavelength-pair nanoscopy with NIR-II continuous-wave laser for multi-chromatic probes. *Nat. Commun.* **2022**, *13* (1), 2843. DOI: 10.1038/s41467-022-30114-z.

(21) Xu, Z.; Chen, L.; Zhang, L.; Jing, S.; Zhuang, B.; Xu, W.; Chen, D. Yb/Er: $Cs_2Ag(In/Bi)Cl_6$ lead-free double perovskite for dual-modal optical temperature sensing. *J. Lumin.* **2022**, *248*, 118996. DOI: 10.1016/j.jlumin.2022.118996.

(22) Wong, K.-L.; Bünzli, J.-C. G.; Tanner, P. A. Quantum yield and brightness. *J. Lumin.* **2020**, *224*, 117256. DOI: 10.1016/j.jlumin.2020.117256.

(23) Kaiser, M.; Würth, C.; Kraft, M.; Hyppänen, I.; Soukka, T.; Resch-Genger, U. Power-dependent upconversion quantum yield of $NaYF_4$:Yb^{3+},Er^{3+} nano- and micrometer-sized particles – measurements and simulations. *Nanoscale* **2017**, *9* (28), 10051-10058. DOI: 10.1039/c7nr02449e.

(24) Arppe, R.; Hyppänen, I.; Perälä, N.; Peltomaa, R.; Kaiser, M.; Würth, C.; Christ, S.; Resch-Genger, U.; Schäferling, M.; Soukka, T. Quenching of the upconversion luminescence of $NaYF_4$:Yb^{3+},Er^{3+} and $NaYF_4$:Yb^{3+},Tm^{3+} nanophosphors by water: the role of the sensitizer Yb^{3+} in non-radiative relaxation. *Nanoscale* **2015**, *7* (27), 11746-11757. DOI: 10.1039/C5NR02100F.

(25) Qiu, H.; Yang, C.; Shao, W.; Damasco, J.; Wang, X.; Ågren, H.; Prasad, P. N.; Chen, G. Enhanced Upconversion Luminescence in Yb^{3+}/Tm^{3+}-Codoped Fluoride Active Core/Active Shell/Inert Shell Nanoparticles through Directed Energy Migration. *Nanomaterials* **2014**, *4* (1), 55-68. DOI: 10.3390/nano4010055.

(26) Zhou, Y.; Cheng, Y.; Xu, J.; Lin, H.; Wang, Y. Thermo-enhanced upconversion luminescence in inert-core/active-shell UCNPs: the inert core matters. *Nanoscale* **2021**, *13* (13), 6569-6576. DOI: 10.1039/D1NR00752A.

(27) Ren, H.; Bai, R.; Liu, C.; Zhang, J.; Wang, L. Quantitative evaluation for the contribution of each component in $NaYF_4$: Yb, Tm@$NaYF_4$: Yb, Ho@$NaYF_4$ upconversion nanoparticle: Active shell, inert shell, size, and their cooperation. *J. Lumin.* **2023**, *263*, 120057. DOI: 10.1016/j.jlumin.2023.120057.

(28) Wang, P.; Cheng, S.; Xu, Y.; Nie, G.; Zhan, S.; Liu, Y. Upconversion nanoparticles with active shell exhibit high thermometry sensitivity in water. *Mater. Res. Bull.* **2023**, *162*, 112190. DOI: 10.1016/j.materresbull.2023.112190.

(29) Shahsavar Gocmen, M.; Dulda, A. Boosting NIR emission through Yb concentration optimization in active-core/active shell upconversion nanocrystals. *Opt. Mater.* **2024**, *152*, 115519. DOI: 10.1016/j.optmat.2024.115519.

(30) Wen, S.; Zhou, J.; Zheng, K.; Bednarkiewicz, A.; Liu, X.; Jin, D. Advances in highly doped upconversion nanoparticles. *Nat. Commun.* **2018**, *9* (1), 2415. DOI: 10.1038/s41467-018-04813-5.

(31) Kuang, Y.; Xu, J.; Wang, C.; Li, T.; Gai, S.; He, F.; Yang, P.; Lin, J. Fine-Tuning Ho-Based Red-Upconversion Luminescence by Altering $NaHoF_4$ Core Size and $NaYbF_4$ Shell Thickness. *Chem. Mater.* **2019**, *31* (19), 7898-7909. DOI: 10.1021/acs.chemmater.9b01944.

(32) Mun, K. R.; Kyhm, J.; Lee, J. Y.; Shin, S.; Zhu, Y.; Kang, G.; Kim, D.; Deng, R.; Jang, H. S. Elemental-Migration-Assisted Full-Color-Tunable Upconversion Nanoparticles for Video-Rate Three-Dimensional Volumetric Displays. *Nano Lett.* **2023**, *23* (7), 3014-3022. DOI: 10.1021/acs.nanolett.3c00397.

(33) Gao, W.; Xing, Y.; Chen, B.; Shao, L.; Zhang, J.; Yan, X.; Han, Q.; Zhang, C.; Liu, L.; Dong, J. Enhancing red upconversion emission in $NaErF_4$@$NaYF_4$ core-shell nanoparticles by introducing Yb^{3+} ions as energy trapping centers. *J. Alloys Compd.* **2023**, *936*, 168371. DOI: 10.1016/j.jallcom.2022.168371.

(34) Lin, H.; Cheng, Z.; Xu, D.; Zheng, X.; Ge, J.; Xu, L.; Ma, Y.; Yang, S.; Zhang, Y. Constructing a small core–multishell nanostructure for Ho-based red upconversion emission. *J. Mater. Chem. C* **2021**, *9* (12), 4385-4392. DOI: 10.1039/D1TC00115A.

(35) Zhou, B.; Yang, W.; Han, S.; Sun, Q.; Liu, X. Photon Upconversion Through Tb^{3+}-Mediated Interfacial Energy Transfer. *Adv. Mater.* **2015**, *27* (40), 6208-6212. DOI: 10.1002/adma.201503482.

(36) Liu, S. S.; Xu, Z.; Zhao, S. L.; Liang, Z. Q.; Zhu, W. Effects of F^- Concentration on the Morphologies and Fluorescent Lifetimes of Ln^{3+}-Doped Up-Conversion Nanocrystals. *Acta Phys.-Chim. Sin.* **2016**, *32* (8), 2108-2112.

DOI: 10.3866/PKU.WHXB201605091.

(37) Lyu, Z.-Y.; Dong, H.; Yang, X.-F.; Huang, L.; Xu, Y.-J.; Wu, K.; Sun, L.-D.; Yan, C.-H. Phase-Transition-Driven Regional Distribution of Rare-Earth Ions for Multiplexed Upconversion Emissions. *JACS Au* **2023**, *3* (3), 860-867. DOI: 10.1021/jacsau.2c00660.

(38) Wang, F.; Han, Y.; Lim, C. S.; Lu, Y.; Wang, J.; Xu, J.; Chen, H.; Zhang, C.; Hong, M.; Liu, X. Simultaneous phase and size control of upconversion nanocrystals through lanthanide doping. *Nature* **2010**, *463* (7284), 1061-1065. DOI: 10.1038/nature08777.

(39) Feng, Y.; Xiao, Q.; Zhang, Y.; Li, F.; Li, Y.; Li, C.; Wang, Q.; Shi, L.; Lin, H. Neodymium-doped $NaHoF_4$ nanoparticles as near-infrared luminescent/T_2-weighted MR dual-modal imaging agents in vivo. *J. Mater. Chem. B* **2017**, *5* (3), 504-510. DOI: 10.1039/c6tb01961g.

(40) Ni, D.; Bu, W.; Zhang, S.; Zheng, X.; Li, M.; Xing, H.; Xiao, Q.; Liu, Y.; Hua, Y.; Zhou, L.; et al. Single Ho^{3+}-Doped Upconversion Nanoparticles for High-Performance T_2-Weighted Brain Tumor Diagnosis and MR/UCL/CT Multimodal Imaging. *Adv. Funct. Mater.* **2014**, *24* (42), 6613-6620. DOI: 10.1002/adfm.201401609.

(41) Lin, H.; Xu, D.; Cheng, Z.; Li, Y.; Xu, L.; Ma, Y.; Yang, S.; Zhang, Y. Small-sized red-emitting core/shell/shell nanoparticles through an efficient energy back transfer process. *Appl. Surf. Sci.* **2020**, *514*. DOI: 10.1016/j.apsusc.2020.146074.

(42) Kuang, Y.; Yang, D.; Gai, S.; He, F.; An, B.; Yang, P. Uncovering Different Responses and Energy Mechanisms of Sensitizer and Activator in Host Manipulation for Upconversion Nanoparticles. *Inorg. Chem.* **2023**, *62* (27), 10805-10821. DOI: 10.1021/acs.inorgchem.3c01423.

(43) Chen, G.; Liu, H.; Somesfalean, G.; Liang, H.; Zhang, Z. Upconversion emission tuning from green to red in Yb^{3+}/Ho^{3+}-codoped $NaYF_4$ nanocrystals by tridoping with Ce^{3+} ions. *Nanotechnology* **2009**, *20* (38), 385704. DOI: 10.1088/0957-4484/20/38/385704.

(44) Hu, S.; Yuan, M.; Huang, H.; Song, C.; Han, K.; Cui, W.; Yang, Z.; Wang, H. Effect of Ce dopant on upconversion and temperature sensing performances in homogeneous ultrasmall Y_2O_3:Yb^{3+}/Ho^{3+} nanoparticles through flame aerosol synthesis. *Ceram. Int.* **2023**, *49* (7), 10953-10960. DOI: 10.1016/j.ceramint.2022.11.290.

(45) Yi, Z.; Zeng, T.; Xu, Y.; Lu, W.; Qian, C.; Liu, H.; Zeng, S.; Hao, J. Multicolor tuning towards single red-emission band of upconversion nanoparticles for tunable optical component and optical/x-ray imaging agents via Ce^{3+} doping. *Nanotechnology* **2015**, *26* (38), 385702. DOI: 10.1088/0957-4484/26/38/385702.

(46) Kuang, Y.; Li, T.; Jia, T.; Gulzar, A.; Zhong, C.; Gai, S.; He, F.; Yang, P.; Lin, J. Insight into the Luminescence Alternation of Sub-30 nm Upconversion Nanoparticles with a Small $NaHoF_4$ Core and Multi-Gd^{3+}/Yb^{3+} Coexisting Shells. *Small* **2020**, *16* (43), 2003799. DOI: https://doi.org/10.1002/smll.202003799.

(47) Watanabe, S.; Asanuma, T.; Sasahara, T.; Hyodo, H.; Matsumoto, M.; Soga, K. 3D Micromolding of Arrayed Waveguide Gratings on Upconversion Luminescent Layers for Flexible Transparent Displays without Mirrors, Electrodes, and Electric Circuits. *Adv. Funct. Mater.* **2015**, *25* (28), 4390-4396. DOI: https://doi.org/10.1002/adfm.201500542.

(48) Ding, M.; Lu, C.; Ni, Y.; Xu, Z. Rapid microwave-assisted flux growth of pure β-$NaYF_4$:Yb^{3+}, Ln^{3+} (Ln=Er, Tm, Ho) microrods with multicolor upconversion luminescence. *Chem. Eng. J.* **2014**, *241*, 477-484. DOI: https://doi.org/10.1016/j.cej.2013.10.045.

(49) Joshi, R.; Patra, S.; Srivastava, M.; Singh, B. P.; Chakraborty, A.; Shelar, S. B.; Chakravarty, R.; Chakraborty, S.; Ningthoujam, R. S. Mesoporous $NaGdF_4$/Ho–Yb@m-SiO_2 Upconversion Nanophosphors as a Potent Theranostic Probe. *ACS Appl. Nano Mater.* **2022**, *5* (9), 12962-12971. DOI: 10.1021/acsanm.2c02782.

(50) Li, H.; Hao, S. W.; Yang, C. H.; Chen, G. Y. Synthesis of Multicolor Core/Shell $NaLuF_4$:Yb^{3+}/Ln^{3+}@CaF_2 Upconversion Nanocrystals. *Nanomaterials* **2017**, *7* (2), 34. DOI: 10.3390/nano7020034.

(51) Gao, W.; Cheng, X.; Xing, Y.; Han, S.; Chen, B.; Han, Q.; Yan, X.; Liu, J.; Liu, L.; Dong, J. Enhancement of

red upconversion emission intensity of Ho^{3+} ions in $NaLuF_4$:Yb^{3+}/Ho^{3+}/Ce^{3+}@$NaLuF_4$ core–shell nanoparticles. *J. Rare Earths* **2022**, *40* (4), 517-525. DOI: https://doi.org/10.1016/j.jre.2021.11.005.

(52) Huang, H.; Wang, S.; Chen, R.; Zhang, N.; Yao, H.-R.; Zheng, Y.; Huang, F.; Chen, D. Engineering upconverting core-shell nano-probe for spectral responsive fluid velocimetry. *Nano Res.* **2023**, *16* (1), 1212-1219. DOI: 10.1007/s12274-022-4636-4.

(53) Liao, H.; Ye, S.; Xu, X.; Lin, P.; Pan, L.; Wang, D. Dual excitable upconversion nanoparticle@polydopamine nanocomposite with intense red emission and efficient photothermal generation. *J. Rare Earths* **2023**, *41* (12), 1860-1868. DOI: https://doi.org/10.1016/j.jre.2022.12.008.

(54) Lv, F.; La, J.; He, S.; Liu, Y.; Huang, Y.; Wang, Y.; Wang, W. Off-Angle Amplified Spontaneous Emission of Upconversion Nanoparticles by Propagating Lattice Plasmons. *ACS Appl. Mater. Interfaces* **2022**, *14* (48), 54304-54312. DOI: 10.1021/acsami.2c13385.

(55) Chen, G. Y.; Liu, H. C.; Somesfalean, G.; Liang, H. J.; Zhang, Z. G. Upconversion emission tuning from green to red in Yb^{3+}/Ho^{3+}-codoped $NaYF_4$ nanocrystals by tridoping with Ce^{3+} ions. *Nanotechnology* **2009**, *20* (38), 385704. DOI: 10.1088/0957-4484/20/38/385704.

(56) Gao, W.; Zheng, H.; Han, Q.; He, E.; Gao, F.; Wang, R. Enhanced red upconversion luminescence by codoping Ce^{3+} in β-NaY($Gd_{0.4}$)F_4:Yb^{3+}/Ho^{3+} nanocrystals. *J. Mater. Chem. C* **2014**, *2* (27), 5327-5334. DOI: 10.1039/C4TC00585F.

(57) Chen, D.; Liu, L.; Huang, P.; Ding, M.; Zhong, J.; Ji, Z. Nd^{3+}-Sensitized Ho^{3+} Single-Band Red Upconversion Luminescence in Core–Shell Nanoarchitecture. *J. Phys. Chem. Lett.* **2015**, *6* (14), 2833-2840. DOI: 10.1021/acs.jpclett.5b01180.

(58) Nadort, A.; Zhao, J.; Goldys, E. M. Lanthanide upconversion luminescence at the nanoscale: fundamentals and optical properties. *Nanoscale* **2016**, *8* (27), 13099-13130. DOI: 10.1039/C5NR08477F.

(59) Zhong, Y.; Rostami, I.; Wang, Z.; Dai, H.; Hu, Z. Energy Migration Engineering of Bright Rare-Earth Upconversion Nanoparticles for Excitation by Light-Emitting Diodes. *Adv. Mater.* **2015**, *27* (41), 6418-6422. DOI: https://doi.org/10.1002/adma.201502272.

Graphical abstract

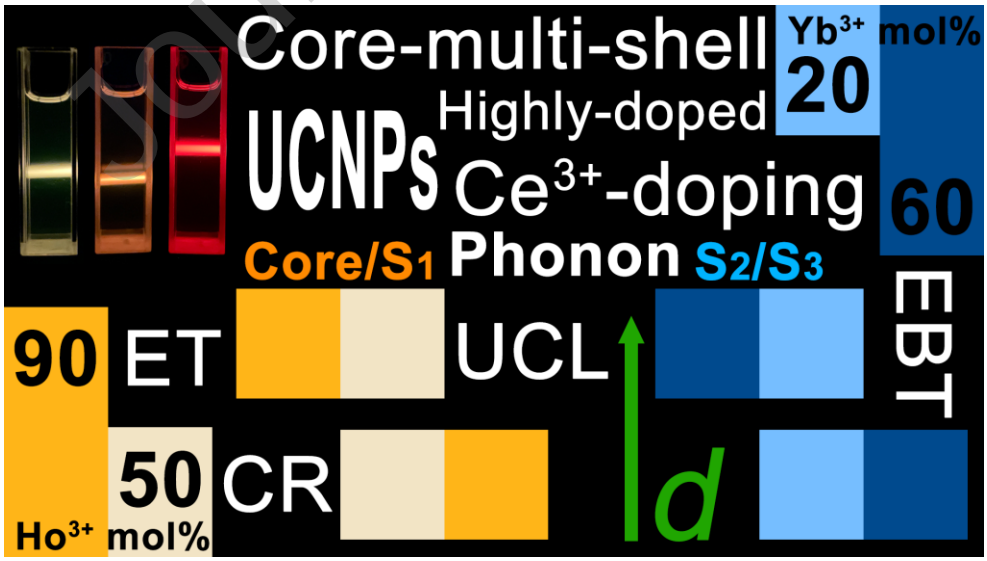

Ho^{3+} and Yb^{3+} concentration distributions in core and the 1st–3rd shells (S_1–S_3) can alter *d* (within which emission were relatively effective) in highly-doped core-multi-shell UCNPs with Ce^{3+} doping,

thus influencing energy mechanisms involving phonon energy, cross-relaxation (CR), energy transfer (ET), energy-back-transfer (EBT), etc., and finetuning UCL properties.

Declaration of interests

☒ The authors declare that they have no known competing financial interests or personal relationships that could have appeared to influence the work reported in this paper.

☐ The authors declare the following financial interests/personal relationships which may be considered as potential competing interests:

Highlights:

- Ce^{3+}-fine-tuned Ho-based upconversion luminescence (UCL) and energy mechanisms were investigated in highly doped, core–multi-shell upconversion nanoparticles (UCNPs).
- Factors underexplored or difficult to realise in conventional low-doped or co-doped UCNPs were examined for Ce^{3+}-tuned UCL, including the number of shell layers and varied Ho^{3+}, Yb^{3+} and Ce^{3+} concentration distributions in core and different layers.
- The UCL intensities, green-to-red intensity ratios and decay lifetimes of Ce^{3+}-doped UCNPs were effectively tuned through Ho^{3+} and Yb^{3+} distributions in core–multi-shell structures.
- Compared to conventional low-doped UCNPs, our Ce^{3+}-doped UCNPs still demonstrated tunable UCL colour dependent on pump power, offering enhanced application potentials.